Disc-jet coupling changes as a possible indicator for outbursts from GX 339-4 remaining within the X-ray hard state

de Haas, S.E.M.; Russell, T.D.; Degenaar, N.; Markoff, S.; Tetarenko, A.J.; Tetarenko, B.E.; van den Eijnden, J.; Miller-Jones, J.C.A.; Parikh, A.S.; Plotkin, R.M.; Sivakoff, G.R.

DOI
10.1093/mnras/staa3853

Publication date
2021

Document Version
Final published version

Published in
Monthly Notices of the Royal Astronomical Society

Monthly Notices of the ROYAL ASTRONOMICAL SOCIETY

MNRAS **502,** 521–540 (2021) doi:10.1093/mnras/staa3853
Advance Access publication 2020 December 31

Disc–jet coupling changes as a possible indicator for outbursts from GX 339−4 remaining within the X-ray hard state

S. E. M. de Haas,[1,2]★ T. D. Russell,[1,3] N. Degenaar,[1] S. Markoff,[1,2] A. J. Tetarenko,[4] B. E. Tetarenko,[5] J. van den Eijnden,[1,6] J. C. A. Miller-Jones,[7] A. S. Parikh,[1] R. M. Plotkin[8] and G. R. Sivakoff[9]

[1]*Anton Pannekoek Institute for Astronomy, University of Amsterdam, Science Park 904, NL-1098 XH Amsterdam, the Netherlands*
[2]*Gravitation Astroparticle Physics Amsterdam (GRAPPA) Institute, University of Amsterdam, Science Park 904, NL-1098 XH Amsterdam, the Netherlands*
[3]*INAF, Istituto di Astrofisica Spaziale e Fisica Cosmica, Via U. La Malfa 153, I-90146 Palermo, Italy*
[4]*East Asian Observatory, 660 N. A'ohōkū Place, University Park, Hilo, HI 96720, USA*
[5]*Department of Astronomy, University of Michigan, 1085 South University Avenue, Ann Arbor, MI 48109, USA*
[6]*Astrophysics, Department of Physics, University of Oxford, Denys Wilkinson Building, Keble Road, Oxford OX1 3RH, UK*
[7]*International Centre for Radio Astronomy Research - Curtin University, GPO Box U1987, Perth, WA 6845, Australia*
[8]*Department of Physics, University of Nevada, Reno, NV 89557, USA*
[9]*Department of Physics, University of Alberta, CCIS 4-181, Edmonton, AB T6G 2E1, Canada*

Accepted 2020 December 4. Received 2020 December 3; in original form 2020 September 30

ABSTRACT

We present quasi-simultaneous radio, (sub-)millimetre, and X-ray observations of the Galactic black hole X-ray binary GX 339−4, taken during its 2017–2018 outburst, where the source remained in the hard X-ray spectral state. During this outburst, GX 339−4 showed no atypical X-ray behaviour that may act as an indicator for an outburst remaining within the hard state. However, quasi-simultaneous radio and X-ray observations showed a flatter than expected coupling between the radio and X-ray luminosities (with a best-fitting relation of $L_{\rm radio} \propto L_{\rm X}^{0.39\pm0.06}$), when compared to successful outbursts from this system ($L_{\rm radio} \propto L_{\rm X}^{0.62\pm0.02}$). While our 2017–2018 outburst data only span a limited radio and X-ray luminosity range (∼1 order of magnitude in both, where more than 2 orders of magnitude in $L_{\rm X}$ is desired), including data from other hard-only outbursts from GX 339−4 extends the luminosity range to ∼1.2 and ∼2.8 orders of magnitude, respectively, and also results in a flatter correlation (where $L_{\rm radio} \propto L_{\rm X}^{0.46\pm0.04}$). This result is suggestive that for GX 339−4 a flatter radio–X-ray correlation, implying a more inefficient coupling between the jet and accretion flow, could act as an indicator for a hard-only outburst. However, further monitoring of both successful and hard-only outbursts over larger luminosity ranges with strictly simultaneous radio and X-ray observations is required from different single sources to explore if this applies generally to the population of black hole X-ray binaries, or even GX 339−4 at higher hard-state luminosities.

Key words: accretion, accretion discs – black hole physics – stars: individual: GX 339−4, outflows – X-rays: binaries.

1 INTRODUCTION

Black hole (BH) low-mass X-ray binaries (LMXBs) are systems where material from a low-mass ($< 3\,M_{\odot}$) donor star is transferred to a stellar-mass black hole via Roche lobe overflow. The infalling matter forms a differentially rotating accretion disc (e.g. Pringle, Rees & Pacholczyk 1973) and material is partially accreted on to the BH, while the remaining fraction may be ejected from the system via outflows in the form of relativistic jets (e.g. Mirabel et al. 1992; Fender 2001) or disc winds (e.g. Ponti et al. 2012; Díaz Trigo & Boirin 2016). LMXBs are ideal objects for studying accretion and jet physics as they evolve on observable (month-year) time-scales, providing a time-resolved view of their evolution through their outburst duty cycles (which, are phases of increased accretion on to the BH) and the connection between the inflow and outflow as they evolve (e.g. Fender 2010). These objects also allow us to observe their interaction with their surroundings (e.g. Corbel & Fender 2002; Corbel et al. 2004; Gallo et al. 2005; Mirabel et al. 2011; Justham & Schawinski 2012; Rushton et al. 2017; Tetarenko et al. 2018; Russell et al. 2019b; Bright et al. 2020; Tetarenko et al. 2020).

BH LMXBs emit across the electromagnetic spectrum, where the near-Infrared (IR) and optical to X-ray radiation typically originates from the in-flowing material (often with some contribution from the companion star or disc winds), while the radio, millimetre (mm) and far-infrared emission is generally radiated by the jet (e.g. Fender 2001; Russell et al. 2013, 2014; Tetarenko et al. 2015). These objects spend the majority of their lifetimes in a low-luminosity quiescent state (with X-ray luminosities of $\lesssim 10^{-5}\,L_{\rm Edd}$; Plotkin, Gallo & Jonker 2013). However, they may go through episodic phases of outburst that typically last months to ∼a year, during which their luminosities can increase by orders of magnitude due to an increase in the mass-accretion rate on to the BH (see, e.g. McClintock & Remillard 2006; Corral-Santana et al. 2016; Tetarenko et al. 2016).

During quiescence and the early rise phase of an outburst, the system is typically in the hard accretion state. In this state, the

★ E-mail: sebastiaan.dehaas@student.uva.nl

observed X-ray spectrum is dominated by a power-law component, thought to arise from inverse Compton emission originating in a geometrically thick, optically thin, radiatively inefficient accretion flow (RIAF; e.g. Narayan & Yi 1995; Esin, McClintock & Narayan 1997), or possibly the base of the jet (e.g. Markoff, Nowak & Wilms 2005; Maitra et al. 2009; Connors et al. 2019; Lucchini et al. 2019). The quiescent and hard state are associated with a steady, partially self-absorbed compact jet (e.g. Fender, Belloni & Gallo 2004) exhibiting a flat-to-inverted radio to (sub-)mm spectrum (e.g. Corbel et al. 2000; Dhawan, Mirabel & Rodríguez 2000; Fender 2001; Russell et al. 2014, 2015; Tetarenko et al. 2015, Plotkin et al. 2017; Dinçer et al. 2018), which can extend up to and beyond the IR band (e.g. Russell et al. 2013). For such a spectrum, the radio flux density S_ν is proportional to the frequency ν such that $S_\nu \propto \nu^\alpha$, where the spectral index $\alpha \gtrsim 0$ (e.g. Fender 2006).

As a typical outburst progresses, it is generally thought that material that has built in the outer disc up over time reaches a critical point, following which, material can then flow in towards the BH, causing the source to source brighten (e.g. Lasota 2001). During this phase, the X-ray spectrum progressively softens as the X-ray emission becomes increasingly dominated by a multitemperature blackbody component from the hot inner regions of an optically thick, geometrically thin accretion disc. As a consequence, the system may enter and transit through the hard intermediate and soft intermediate X-ray states (HIMS and SIMS, respectively; e.g. Remillard & McClintock 2006; Belloni 2010), entering the full soft state as the disc completely dominates the observed X-ray emission. At some point during this progression, the compact jet emission is strongly quenched (by >3.5 orders of magnitude; Russell et al. 2019b) and discrete ejecta may be launched in a transient jet (e.g. Mirabel & Rodríguez 1994; Hjellming & Rupen 1995; Fender 2006). These transient jet ejecta are thought to be composed of steep spectrum ($\alpha \approx -0.7$) discrete, synchrotron emitting plasma that are propagating away from the BH at relativistic speeds (e.g. Tingay et al. 1995; Fender, Homan & Belloni 2009; Tetarenko et al. 2017) and typically manifest as rapid flaring activity in time-resolved light curves.

Following the spectral transition, the luminosity drops as the mass accretion rate on to the compact object reduces and the outburst fades. As the source decays it transits back through the intermediate states to the hard state in a reverse transition (e.g. Narayan, McClintock & Yi 1996; Hameury et al. 1997). During this progression, the compact jet switches back on progressively (over a period of a few weeks; e.g. Miller-Jones et al. 2012; Corbel et al. 2013b; Kalemci et al. 2013; Russell et al. 2014).

However, not all outbursts follow this typical 'successful' progression. Instead, outbursts can exhibit multiple peaks, re-brightenings, or glitches (e.g. Chen, Shrader & Livio 1997), during which the connection to the jet is not well understood (e.g. Parikh et al. 2019). Some outbursts fail to enter the soft state, such that the source remains in the hard X-ray spectral state (e.g. Harmon et al. 1994; Hynes et al. 2000; Brocksopp et al. 2001; Belloni et al. 2002; Aref'ev et al. 2004; Brocksopp, Bandyopadhyay & Fender 2004; Sturner & Shrader 2005; Brocksopp et al. 2010; Sidoli et al. 2011; Curran & Chaty 2013) or only progresses as far as the intermediate states during the outburst (e.g. in't Zand et al. 2002; Wijnands & Miller 2002; Capitanio et al. 2009; Ferrigno et al. 2012; Reis et al. 2012; Soleri et al. 2013; Zhou et al. 2013; Curran et al. 2014). These outbursts are generally referred to as 'hard-only' outbursts and it is not well understood why some outbursts do not progress to a soft state. One possible explanation is that hard-only outbursts are a result of less disc material being able to flow into the inner regions of the accretion disc, such that a full outburst cannot be sustained. As would be implied by such a scenario, hard-only outbursts are typically fainter on-average than successful outbursts (Tetarenko et al. 2016), indicating lower peak accretion rates. Additionally, hard-only outbursts are shorter in duration, lasting on average ∼247 d compared to ∼391 d for successful outbursts (Tetarenko et al. 2016).

In the hard states of BH LMXB outbursts, there is an observed correlation between the radio luminosity (L_r) and X-ray luminosity (L_X). This correlation holds over a few orders of magnitude in luminosity, and can be used to investigate the disc–jet coupling (e.g. Hannikainen, Hunstead & Campbell-Wilson 1998; Corbel et al. 2000, 2003, 2013a; Gallo, Fender & Pooley 2003; Gallo, Miller & Fender 2012; Gallo, Degenaar & van den Eijnden 2018). The observed correlation is nonlinear and typically divided by two separate tracks, the upper 'standard' track and a lower, shallower one, although the statistical significance of the need for two different tracks is debated (Gallo et al. 2014, 2018). It has also been suggested that the difference between the two slopes may be related to the observed jet emission (e.g. Casella & Pe'er 2009; Coriat et al. 2011; Meyer-Hofmeister & Meyer 2014; Espinasse & Fender 2018). According to Gallo et al. (2012), for the full sample of standard track BH LMXBs, the radio luminosity correlates with X-ray luminosity as $L_\mathrm{r} \propto L_\mathrm{X}^{0.63\pm0.03}$. Using only data from GX 339−4 over multiple outbursts (including both successful and hard-only outbursts), Corbel et al. (2013a) reported a relation of $L_\mathrm{r} \propto L_\mathrm{X}^{0.62\pm0.01}$. However, Corbel et al. (2013a) show that over limited X-ray luminosity ranges (<2 orders of magnitude) individual outbursts can show significant deviation from the source's typical correlation.

In this paper we present X-ray, radio and (sub-)mm monitoring of the Galactic BH LMXB GX 339−4 during its 2017–2018 hard-only outburst. In Section 2 we describe the observational setup and data used. Section 3 presents the results from the radio, (sub-)mm, and X-ray monitoring. In Section 4, we discuss and compare the results: exploring the X-ray spectral evolution, in particular the source hardness and X-ray photon index (Γ), as well as the behaviour of the radio jet. We also attempt to physically explain the observed evolution of this outburst. Finally, we compare our results to other outbursts of GX 339−4, both hard-only and successful, searching for any X-ray or radio signatures that may act as indicators for an outburst only remaining in the hard or intermediate states and not progressing into the soft state. Conclusions are provided in Section 5. All radio, (sub-)mm, and X-ray results are presented throughout the paper and in the Appendices.

1.1 GX 339−4

GX 339−4 is an LMXB with a BH primary (e.g. Hynes et al. 2003), that has a mass of $2.3\,\mathrm{M}_\odot < M_\mathrm{BH} < 9.5\,\mathrm{M}_\odot$ (Heida et al. 2017). This system exhibits a 1.76 d orbital period and has a K-type companion star. The distance to the source is still a matter of debate, with estimates ranging from ∼5–12 kpc (e.g. Zdziarski et al. 2004; Heida et al. 2017; Zdziarski, Ziółkowski & Mikołajewska 2019). GX 339−4 was first discovered by the Massachusetts Institute of Technology (MIT) X-ray detector on the *Orbiting Solar Observatory 7* satellite in 1972, and was first detected in the radio band in 1994 by the Molonglo Observatory Synthesis Telescope at 843 MHz (Sood & Campbell-Wilson 1994). Undergoing numerous successful and hard-only outbursts over the past few decades (so far 41 per cent from a total of 22 detected outbursts have been identified as hard-only; Tetarenko et al. 2016), GX 339−4 is one of the best studied BH LMXBs (e.g. Zdziarski et al. 2004; Buxton et al. 2012), particularly at both radio and X-ray wavelengths (e.g. Corbel et al. 2013a).

Table 1. X-ray evolution of GX 339−4 during its 2017–2018 hard-only outburst. These parameters were determined from *Swift*-XRT monitoring, where $N_{\rm H} = (0.56 \pm 0.02) \times 10^{22}$ cm^{-2}, which was tied and jointly fit across all epochs of this outburst. The total χ^2 for the joint fit is 2129.36 with 2139 degrees of freedom. Errors are 1σ.

Date	MJD	ObsID	Count rate	Γ	Normalization	Unabsorbed flux (0.5–10 keV) $\times 10^{-10}$ erg s^{-1} cm^{-2}	Hardness (1.5–10 keV / 0.5–1.5 keV)
2017–09–29	58025	00032898146	1.20 ± 0.09	1.73 ± 0.15	0.012 ± 0.002	0.73 ± 0.06	$2.61^{+0.75}_{-0.70}$
2017–10–01	58027	00032898148	1.45 ± 0.09	1.20 ± 0.09	0.010 ± 0.001	1.1 ± 0.1	$6.12^{+1.15}_{-1.11}$
2017–10–03	58029	00032898149	1.15 ± 0.11	1.52 ± 0.14	0.018 ± 0.002	1.4 ± 0.1	$3.64^{+0.94}_{-0.88}$
2017–10–05	58031	00032898150	2.53 ± 0.10	1.18 ± 0.08	0.014 ± 0.001	1.64 ± 0.08	$6.30^{+0.96}_{-0.93}$
2017–10–07	58033	00032898151	4.24 ± 0.22	1.24 ± 0.09	0.026 ± 0.003	2.85 ± 0.19	$5.74^{+1.10}_{-1.06}$
2017–10–09	58035	00032898152	5.97 ± 0.25	1.23 ± 0.06	0.039 ± 0.003	4.3 ± 0.2	$5.82^{+0.73}_{-0.71}$
2017–10–17	58043	00032898153	10.71 ± 0.54	1.26 ± 0.08	0.062 ± 0.005	6.6 ± 0.4	$5.54^{+0.90}_{-0.86}$
2017–10–20	58046	00032898154	11.28 ± 0.48	1.30 ± 0.06	0.084 ± 0.006	8.45 ± 0.35	$5.18^{+0.65}_{-0.63}$
2017–10–23	58049	00032898155	14.88 ± 0.15	1.58 ± 0.02	0.130 ± 0.003	9.4 ± 0.1	$3.31^{+0.15}_{-0.14}$
2017–10–25	58051	00032898158	15.76 ± 0.17	1.54 ± 0.03	0.097 ± 0.003	7.3 ± 0.1	$3.50^{+0.19}_{-0.18}$
2017–11–01	58058	00032898160	12.00 ± 0.14	1.45 ± 0.03	0.094 ± 0.003	7.8 ± 0.1	$4.05^{+0.20}_{-0.20}$
2018–01–20	58138	00032898161	5.93 ± 0.21	1.38 ± 0.06	0.041 ± 0.003	3.8 ± 0.2	$4.53^{+0.60}_{-0.58}$
2018–01–25	58143	00032898162	3.84 ± 0.14	1.33 ± 0.09	0.029 ± 0.003	1.33 ± 0.09	$4.94^{+0.86}_{-0.82}$
2018–01–30	58148	00032898163	2.23 ± 0.10	1.23 ± 0.07	0.015 ± 0.001	1.60 ± 0.08	$5.75^{+0.88}_{-0.85}$
2018–02–04	58153	00032898164	1.32 ± 0.10	1.14 ± 0.12	0.007 ± 0.001	0.90 ± 0.08	$6.73^{+1.78}_{-1.69}$
2018–02–07	58156	00032898165	1.47 ± 0.08	1.27 ± 0.09	0.007 ± 0.001	0.69 ± 0.05	$5.40^{+1.03}_{-0.99}$
2018–02–09	58158	00032898166	1.11 ± 0.08	1.34 ± 0.1	0.008 ± 0.001	0.72 ± 0.05	$4.87^{+1.09}_{-1.04}$
2018–02–14	58163	00032898167	0.61 ± 0.04	1.52 ± 0.1	0.0047 ± 0.0004	0.36 ± 0.02	$3.62^{+0.65}_{-0.63}$
2018–02–27	58176	00032898170	0.28 ± 0.02	1.60 ± 0.15	0.0024 ± 0.0003	0.17 ± 0.01	$3.21^{+0.87}_{-0.82}$

Therefore, it is an ideal candidate to probe the disc–jet connection and identify accretion or jet signatures that may indicate whether an outburst will complete a full, successful outburst or not.

2 OBSERVATIONS AND ANALYSIS METHODS

2.1 X-ray analysis

2.1.1 Swift-*XRT*

X-ray observations of GX 339−4 were taken by the Neil Gehrels *Swift* Observatory X-ray telescope (XRT) throughout its 2017–2018 hard-only outburst. We used the *Swift*-XRT online pipeline[1] (Evans et al. 2009) to retrieve pile-up corrected spectral data. To compare behaviours between hard-only events of GX 339−4, we also downloaded observations taken during its 2013 hard-only outburst and 2018–2019 hard-only flare. We note that following this flaring event, while the source faded to almost quiescence, it did not completely return to quiescence before re-brightening in late-2019, going into a full outburst in 2019–2020 (Rao et al. 2019; Paice et al. 2020). Hence, we refer to the 2018–2019 hard-only event as a flare as opposed to a full outburst. For the 2017–2018 outburst, all *Swift*-XRT data were obtained in photon counting (PC) mode. While data from the 2013 hard-only outburst and 2018–2019 hard-only flare were mostly obtained in the PC mode, some observations were taken in *Swift*-XRT's windowed timing (WT) mode.

Since the focus of this work is the 2017–2018 outburst, only the epochs of this outburst will be discussed in detail, but we show all X-ray data and fitting parameters in the Appendix. The 2017–2018 *Swift*-XRT data of this outburst consisted of 19 observations taken between 2017–09–29 (MJD 58025) and 2018–02–27 (MJD 58176), see Table 1. However, from the beginning of November 2017 until mid-January 2018, constraints due to the proximity of the Sun prevented *Swift*-XRT from obtaining data of GX 339−4.

The data were analysed using XSPEC (version 12.8; Arnaud 1996) from HEASOFT software package (version 6.21). The 0.5–10 keV X-ray spectra were modelled with an absorbed power-law (TBABS×POWERLAW) within XSPEC. The `tbabs` model component, making use of abundances from Wilms, Allen & McCray 2000, and photoionization cross-sections from Verner et al. (1996), was used to account for interstellar absorption. Tying the line-of-sight equivalent hydrogen absorption, $N_{\rm H}$, across all epochs provided $N_{\rm H} = (0.56 \pm 0.02) \times 10^{22}$ cm^{-2}. We also compared all results with $N_{\rm H}$ either fixed to literature values ($N_{\rm H,\,fixed} = 0.851 \times 10^{22}$ cm^{-2}; Fürst et al. 2015), or left free (untied) for all epochs, finding our conclusions were not altered by the method that was used.

X-ray fluxes were determined using the convolution model `cflux` within XSPEC. The X-ray fluxes were measured for four different energy bands, namely 1–10 keV, 0.5–10 keV, 0.5–1.5 keV and 1.5–10 keV.

For our X-ray analysis, the X-ray luminosity, $L_{\rm X}$, was calculated as $L_{\rm X} = 4\pi F_{\rm X} D^2$, where $F_{\rm X}$ is the X-ray flux and D is the source distance. In this work, we adopt a source distance of 8 kpc (Zdziarski et al. 2004, 2019; Heida et al. 2017).

2.1.2 MAXI

The *Monitor of All-sky X-ray Image* (*MAXI*) X-ray telescope (Matsuoka et al. 2009) count rates (Fig. 1) were obtained from the *MAXI*

[1] https://www.swift.ac.uk/user_objects/

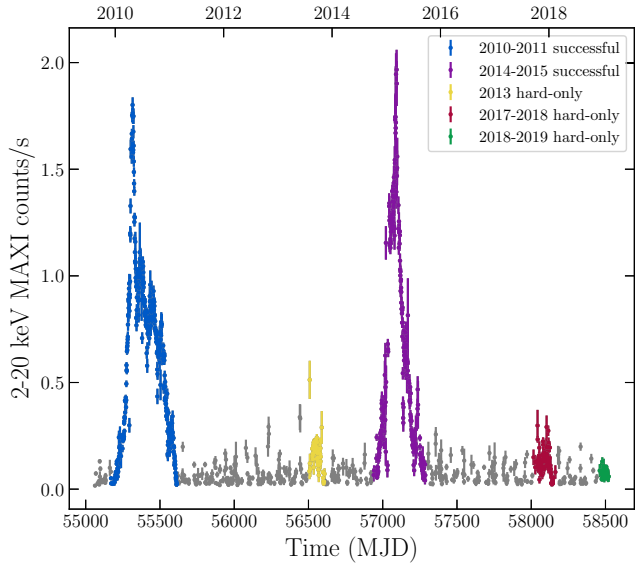

Figure 1. 2–20 keV *MAXI* light curve of GX 339−4 from August 2009 to February 2019, where five outbursts of this source have been highlighted in different colours. During this period, the three hard-only events were significantly less luminous than both successful outbursts and the 2018–2019 hard-only flare was especially faint in this X-ray band.

Table 2. 1–10 keV X-ray fluxes and luminosities determined from the *MAXI* count rates on dates where there was an ATCA radio observation and GX 339−4 was sun constrained to *Swift*-XRT. The 1–10 keV X-ray fluxes and luminosities were estimated from the 2–20 keV *MAXI* count rate by assuming an absorbed powerlaw with $N_{\rm H} = (0.56 \pm 0.02) \times 10^{22}$ cm^{-2} and X-ray photon index of 1.5–2.5. To calculate the luminosity, we assumed a distance of 8 kpc (Zdziarski et al. 2019).

Date	MJD	Count rate (2–20 keV) (counts s^{-1})	Flux (1–10 keV) $\times 10^{-10}$ erg s^{-1} cm^{-2}	Luminosity (1–10 keV) $\times 10^{37}$ erg s^{-1}
2017–11–23	58080	0.169 ± 0.031	24.8 ± 5.5	1.90 ± 0.42
2017–12–03	58090	0.139 ± 0.048	20.4 ± 4.5	1.56 ± 0.35
2017–12–16	58103	0.353 ± 0.052	52.0 ± 11.5	3.98 ± 0.88
2019–01–05	58123	0.142 ± 0.016	21.0 ± 4.6	1.61 ± 0.35

website.[2] During times when *Swift*-XRT was sun constrained but radio observations were taken (MJDs 58080, 58090, 58103, and 58123), we used the *MAXI* count rates to estimate the X-ray flux and luminosity (using WebPIMMS[3]). To do this, we used the $N_{\rm H}$ found from our *Swift*-XRT analysis ($N_{\rm H} = (0.56 \pm 0.02) \times 10^{22}$ cm^{-2}), and assumed Γ to be 1.5–2.5, conservatively estimating the 1–10 keV X-ray flux from the 2–20 keV *MAXI* count rate (Table 2). We do note that the unknown values of Γ may make these fluxes unreliable, however, the range taken for Γ provides a conservative estimate when taking into account the lack of dramatic changes to the X-ray count rate over this time (Fig. 2) and the minimal variation of Γ during other hard-only outbursts from this source (during the brighter phase of the outburst, see Section 4.2.1).

[2]http://maxi.riken.jp/top/index.html
[3]https://heasarc.gsfc.nasa.gov/cgi-bin/Tools/w3pimms/w3pimms.pl

2.2 ATCA radio data

During the 2017–2018 outburst, GX 339−4 was observed 9 times with the Australia Telescope Compact Array (ATCA; PI: Russell, project code: C3057). Observations were carried out at central frequencies of 5.5 and 9 GHz on all dates and additionally at 17 and 19 GHz on five dates, see Table 3. Each frequency pair (5.5/9 or 17/19 GHz) was recorded simultaneously, with a bandwidth of 2 GHz at each frequency band, which was comprised of 2048 channels of width 1 MHz. Observations had 10 second integration times. PKS 1934–638 was used for primary flux and bandpass calibration, while the nearby source PKS 1646–50 was used for phase calibration. Data calibration was carried out following standard procedures from the Common Astronomy Software Application (CASA, version 4.7.1; McMullin et al. 2007[4]). Each frequency band was imaged with natural weighting to maximize sensitivity. The signal-to-noise ratio was not high enough for reliable self-calibration. To determine the radio flux density, S_ν, of the source for each epoch, we fit for a point source in the image plane, where we use a Gaussian with a full width at half-maximum (FWHM) equal to the synthesized beam of the observation. Errors on the absolute flux density scale include systematic uncertainties of 2 per cent for the 5.5/9 GHz data[5] (e.g. Massardi et al. 2011; McConnell et al. 2012) and 4 per cent for the 17/19 GHz data (see, e.g. Murphy et al. 2010; Partridge et al. 2016). All radio flux densities are reported in Table 3.

The radio luminosity ($L_{\rm r}$) was calculated using $L_{\rm r} = 4\pi\nu S_\nu D^2$. Radio spectral indices (α, where $S_\nu \propto \nu^\alpha$; Fender 2001) have been determined by Monte Carlo fitting using all the radio bands that were available for each date.

We also used UVMULTIFIT (Martí-Vidal et al. 2014) to search for source intra-observational variability in the 5.5 and 9 GHz observations. Unfortunately, the setup of the radio observations – where the 10–15 min scans of GX 339−4 were taken sparsely during the full radio observation[6] – meant that the source was not densely sampled during the observation. Additionally, ATCA is a 6-element linear array meaning that the limited instantaneous uv-coverage did not allow variability shorter than 5-min intervals to be tested. For each time interval, we used UVMULTIFIT to fit for a point source (which is a delta function in the uv-plane) at the target position (as well as all other sources in the field when detectable). Results for each variable epoch are provided in Appendix B, in Table B1 and Fig. B1.

2.3 ALMA (sub)-millimetre data

The Atacama Large Millimetre/Sub-Millimetre Array (ALMA) observed GX 339–4 (PI: Tetarenko, project code: 2017.1.00864.T) on 2017 October 5 (21:23:05.0–23:04:36.3 UTC; MJD 58031.8910–58031.9615). Data were taken sequentially in Bands 3, 4, and 6, at central frequencies of 97.5, 145, and 233 GHz, respectively. The ALMA correlator was set up to yield 4 × 2 GHz wide base-bands at each frequency band. During our observations, the 12 m array was in its Cycle 5 C41-9 configuration, with 41 antennas, spending ∼ 8.1/9.8/15.7 min total on the target source in Bands 3, 4, and 6, respectively. The median precipitable water vapour (PWV) during the observations was 0.78, 0.71, and 0.67 mm for the Bands 3, 4, and 6 observations, respectively. All of the data were reduced and imaged within CASA (version 5.1.1; McMullin et al. 2007), using standard

[4]https://casaguides.nrao.edu/index.php?title = Main_Page
[5]https://www.atnf.csiro.au/observers/memos/d96783~1.pdf
[6]Which was generally focused on a different source of interest.

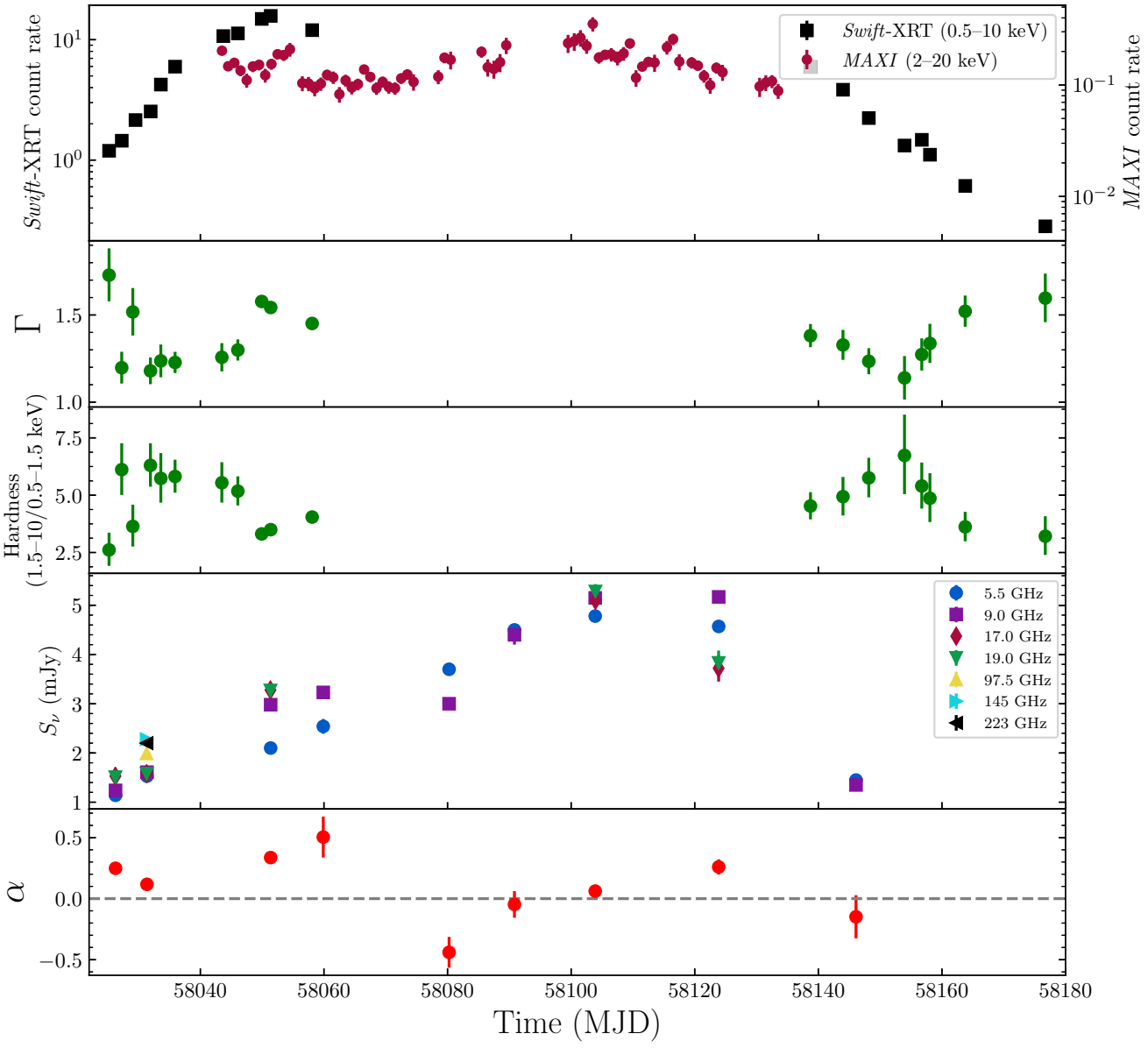

Figure 2. X-ray and radio light curves of GX 339−4 during its 2017–2018 hard-only outburst. Top panel: The 0.5–10 keV and 2–20 keV X-ray count rate evolution during the outburst, where the black squares are determined from *Swift*-XRT and the red circles are from *MAXI* when the source was Sun-constrained to *Swift*-XRT (for clarity, only 5σ *MAXI* detections are shown). Second panel): X-ray photon index, Γ, from the *Swift*-XRT monitoring. (Third panel): X-ray hardness, defined as 1.5–10 keV flux/0.5–1.5 keV flux. Fourth panel: Radio and (sub-)mm flux densities, S_ν. Fifth panel: Radio spectral index, α. GX 339−4 was sun constrained to *Swift*-XRT during the middle of this hard-only outburst.

procedures outlined in the CASAGuides for ALMA data reduction.[7] We used J1617–5848/J1427–4206 as bandpass & flux calibrators, J1650–5044 as a phase calibrator, and J1631–5256 as a check source, for all the observations. To image the continuum emission, we performed multi-frequency synthesis imaging on the data using the `tclean` task within CASA, with natural weighting to maximize sensitivity. Flux densities of the source were then measured by fitting a point source in the image plane (using the `imfit` task). All ALMA sub-mm flux densities are recorded in Table 3. Systematic errors were applied to the absolute flux density calibration of the ALMA data, where an uncertainty of 5 per cent is expected for ALMA bands <350 GHz.[8] We also explored the ALMA sub-mm observations for intra-observational variability. Results are discussed in Section 3.2.1, with light curves and the data points provided in Appendix B.

3 RESULTS

3.1 X-ray light curves and spectral evolution

During the 2017–2018 outburst of GX 339−4, the X-ray light curve shows a roughly single rise and decay evolution with an exponential

[7] https://casaguides.nrao.edu/index.php/ALMAguides

[8] https://almascience.eso.org/documents-and-tools/latest/documents-and-tools/cycle8/alma-technical-handbook

Table 3. ATCA radio and ALMA sub-mm flux densities and spectral indices (α) in different GHz bands for the 2017–2018 outburst of GX 339−4. For the ATCA data, each band (5.5, 9.0, 17.0 and 19.0 GHz) has a ±1 GHz range. Reported ALMA data have a bandwidth of 8 GHz. Errors include systematic uncertainties.

Date	MJD	Frequency (GHz)	Flux density (mJy)	α
2017–09–30	58026	5.5	1.14 ± 0.06	0.25 ± 0.05
		9.0	1.24 ± 0.04	
		17.0	1.53 ± 0.06	
		19.0	1.51 ± 0.06	
2017–10–05	58031	5.5	1.53 ± 0.05	0.11 ± 0.03
		9.0	1.61 ± 0.05	
		17.0	1.58 ± 0.06	
		19.0	1.58 ± 0.06	
		97.5	2.0 ± 0.1	
		145.0	2.28 ± 0.11	
		233.0	2.20 ± 0.11	
2017–10–25	58051	5.5	2.1 ± 0.1	0.34 ± 0.04
		9.0	2.98 ± 0.04	
		17.0	3.28 ± 0.13	
		19.0	3.27 ± 0.06	
2017–11–02	58059	5.5	2.54 ± 0.15	0.50 ± 0.17
		9.0	3.23 ± 0.08	
2017–11–23	58080	5.5	3.7 ± 0.1	−0.44 ± 0.13
		9.0	3.00 ± 0.1	
2017–12–03	58090	5.5	4.5 ± 0.1	−0.05 ± 0.11
		9.0	4.4 ± 0.2	
2017–12–16	58103	5.5	4.78 ± 0.06	0.06 ± 0.02
		9.0	5.15 ± 0.07	
		17.0	5.10 ± 0.15	
		19.0	5.28 ± 0.15	
2018–01–05	58123	5.5	4.57 ± 0.05	0.26 ± 0.06
		9.0	5.17 ± 0.07	
2018–01–27	58146	5.5	1.45 ± 0.08	−0.15 ± 0.18
		9.0	1.35 ± 0.08	

decay (Fig. 2, top panel). *Swift*-XRT monitoring showed a peak 0.5–10 keV X-ray flux of $\approx 9.4 \times 10^{-10}$ erg s^{-1} cm^{-2} at MJD 58049. During the Sun constraints to *Swift*, the source brightened, reaching a peak 2–20 keV flux of $\approx 5.2 \times 10^{-9}$ erg s^{-1} cm^{-2} at MJD 58103, which corresponds to a 0.5–10 keV flux of $\approx 7 \times 10^{-9}$ erg s^{-1} cm^{-2} (assuming $\Gamma = 2$).

During the early stages of our X-ray monitoring, the X-ray photon index (Γ) was variable, where we initially detected a softer X-ray photon index ($\Gamma = 1.73 \pm 0.15$), which then hardened (to $\Gamma = 1.20 \pm 0.09$), before softening again (to $\Gamma = 1.52 \pm 0.14$) and then re-hardening (to $\Gamma = 1.18 \pm 0.08$) once again over the space of about a week (Fig. 2, panel 2). After this variable behaviour, Γ then followed a generally standard pattern of evolution for a hard-only outburst, where it only marginally steepened as the outburst brightened, reaching a Γ of ≈ 1.58 at the peak X-ray flux observed by *Swift*-XRT. However, instead of brightening and softening further, the outburst began to fade and the X-ray spectrum hardened.

Once the X-ray flux began to decrease, Γ also started decreasing in a reverse pattern to its behaviour during the rise phase of the outburst, such that Γ hardened to ≈ 1.15 (Fig. 2). Then, similar to the rise phase, at our lowest observed X-ray fluxes (below 9×10^{-11} erg s^{-1} cm^{-2}) the X-ray photon index then softened progressively as the source faded, evolving to $\Gamma \approx 1.6$ by the end of our monitoring. An analysis of the X-ray hardness, where we use the ratio between the 1.5–10 keV and 0.5–1.5 keV X-ray flux, showed a similar pattern of behaviour for the 2017–2018 outburst (Fig. 2, panel 3).

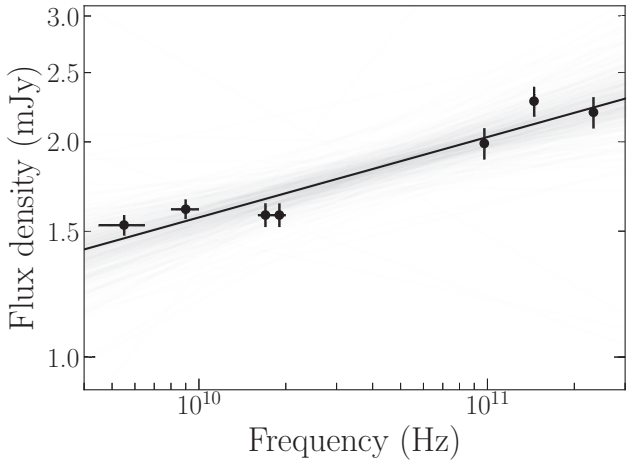

Figure 3. The radio to sub-mm spectrum taken on 2017-10-05 (MJD 58031). Despite the >0.5 d difference between the ATCA and ALMA observations, and the observed source variability, these broad-band data are reasonably well represented by a single power law with a spectral index α of 0.11 ± 0.03 (black line, with errors shown by the fainter grey lines), indicating emission an optically thick compact jet.

3.2 Radio/sub-mm light curves

In our 5-month long radio/sub-mm monitoring of GX 339–4, we observed the integrated radio/sub-mm flux densities vary between ∼1–5 mJy. Long-term light curves revealed a single rise and decay phase (Fig. 2, panel 4), where the spectral index (α) remained flat to inverted (and well represented by a single power law; Fig. 3), except for our radio observation taken on MJD 58080 (Fig. 2, panel 5), which displayed a relatively steep radio spectral index ($\alpha = -0.44 \pm 0.13$). However, as shown below (Section 3.2.1 and Fig. B1), we see a declining trend in the flux density of the radio bands throughout this observation. This is suggestive that the steep spectral index from this epoch could be the result of compact jet variability (where we might expect a delay between variability features of up to tens of minutes between these radio bands, towards the lower frequency band; Tetarenko et al. 2019b). In addition, we do not expect transient ejecta (which tend to show a steep spectrum) to be launched at such a low X-ray luminosity and hard X-ray spectrum, where there does not appear to be any sudden X-ray changes. Therefore, the radio and sub-mm results are consistent with emission from a compact, partially self-absorbed synchrotron jet. This emission remained on for the entire outburst, with no indication of the jet emission being quenched in our observations.

3.2.1 Intra-observational variability

Compact jets have been found to be highly variable on short (<1 d) time-scales (e.g. Tetarenko et al. 2019b). As such, we opted to search for intra-observational variability in our radio through sub-mm data of GX 339–4. Fig. B1 displays intra-observation light curves from the ATCA radio data sampled on 5-min time-scales, while Fig. B2 displays intra-observation light curves from the ALMA sub-mm data sampled on 30-sec time-scales.

To characterize the amplitude of any variability and compare between frequency bands, we use the fractional root mean square (RMS) statistic,

$$F_{\rm var} = \sqrt{\frac{S^2 - \bar{\sigma}_{\rm err}^2}{\bar{x}^2}}, \quad (1)$$

where $\bar{x}$ represents the weighted mean of the flux measurements, the sample variance $S^2 = \frac{1}{N-1}\sum_{i=1}^{N}(x_i - \bar{x})^2$, and the mean square measurement error $\bar{\sigma}_{\rm err}^2 = \frac{1}{N}\sum_{i=1}^{N}\sigma_{{\rm err},i}^2$ (Akritas & Bershady 1996; Vaughan et al. 2003; Sadler et al. 2006). We consider $F_{\rm var}$ < 15 per cent as not significantly variable, 15 per cent < $F_{\rm var}$ < 30 per cent as mildly variable, and $F_{\rm var}$ > 30 per cent as highly variable (as in Tetarenko et al. 2019a).

In the ALMA sub-mm data, we detect clear short-time-scale variability, in the form of structured, small-scale flaring episodes across all three bands sampled. For example, the largest flare detected at 230 GHz (∼ 21:40 UT) is symmetric in shape, and rises to an amplitude of ∼5 times the base flux density level of ∼1 mJy, over a time-scale of ∼2 min (corresponding to a brightness temperature of $\sim 10^8$ K, consistent with other synchrotron events from LMXBs; Pietka, Fender & Keane 2015). We measure fractional RMS values of 21.6 ± 0.1 per cent, 35.9 ± 0.2 per cent, and 35.4 ± 0.1 per cent for the 97, 145, and 230 GHz bands, respectively, indicating a mildly variable to highly variable source at these frequencies. To ensure that the sub-mm variations we observe from GX 339−4 are intrinsic to the source, and not due to atmospheric or instrumental effects, we also extracted intra-observation light curves for our check source. We find that the check source shows relatively constant flux densities throughout our observations in all the bands (with any variations present being <10 per cent of the average flux density), thus we are confident that the variations we observed from GX 339−4 are an accurate representation of the rapidly changing intrinsic flux density of the source.

In the ATCA radio data, we also detected short-time-scale variability. Due to the low-instantaneous uv-coverage of the ATCA interferometric array, we were only able to explore variability down to 5-min time-scales. Additionally, the observing setup meant that only a few 10-min scans of GX 339−4 were taken spread out within a much longer observation. Therefore, our observations do not, and are not as sensitive to, detecting structured flares similar to those we observed within the ALMA sub-mm data. However, we do observe increasing/decreasing trends both within (e.g. 2017-10-05) and throughout some observations (e.g. 2017-09-30, 2017-11-23). This behaviour suggests that small-scale flaring activity, similar to that seen in the sub-mm bands, may have also been occurring in the radio bands, but we were not able to sample the source on short enough time-scales to resolve the flares. We measure fractional RMS values ranging from 1.9–15.8 per cent at 5 GHz and 2.4–17.0 per cent at 9 GHz. While this may indicate a mildly variable source at times, the source was too faint for self-calibration and, therefore, the results may suffer from phase decorrelation or gain drifts. For example, when comparing this variability to a check source present in the ATCA field of view,[9] we find the check source can at times be just as variable as GX 339–4. This, plus the low level of variability, suggests that the radio variations we observe from GX 339–4 may not be completely intrinsic to the source, with possible contributions from atmospheric or instrumental effects.

Comparing the variability properties between the radio and sub-mm bands, we see a pattern of higher variability amplitudes at higher electromagnetic frequencies. This trend is consistent with what we might expect from compact jet emission, as the (sub-)mm emission originates from a region close to the base of the jet (with a smaller cross-section), while the radio emission originates from a region further out in the jet flow (with a large cross-section). Imaging the ALMA data on finer frequency scales (in 2 GHz sub-bands for all bands) shows that the in-band ALMA spectral indices were flat/inverted throughout the observation (Table 4). While these results were time-averaged, they strongly support the suggestion that the observed flux density variations arose from a variable compact jet.

[9]Note that we are only able to detect the check source for the three earliest ATCA observations due to the array configuration changing from a very compact to much more extended configuration on 2017-11-01.

Table 4. ALMA flux densities from each 2 GHz sub-band. The flat-to-inverted (sub-)mm spectrum indicates optically thick emission from a variable compact jet.

Frequency (±2) (GHz)	Flux density (mJy)
90.5	2.0 ± 0.1
92.5	1.9 ± 0.1
102.5	2.1 ± 0.1
104.5	2.1 ± 0.1
138	2.1 ± 0.1
140	2.3 ± 0.1
150	2.5 ± 0.1
152	2.5 ± 0.1
224	2.2 ± 0.1
226	2.2 ± 0.1
240	2.3 ± 0.1
242	2.3 ± 0.1

4 DISCUSSION

4.1 Source brightness

The 2017–2018 hard-only outburst of GX 339−4 was well monitored in the radio and X-ray bands at low X-ray luminosities during the rise phase due to the early discovery of the outburst from regular optical monitoring (Russell, Lewis & Gandhi 2017).[10] As such, our X-ray and radio monitoring began at an X-ray luminosity of $\approx 5.6 \times 10^{35}$ erg s^{-1}, corresponding to an Eddington luminosity, $L_{\rm Edd}$, of $\sim 5.8 \times 10^{-4}$ (assuming a distance of 8 kpc and $M_{\rm BH} = 7.8\,{\rm M}_{\odot}$, which is the peak of the best-fitting mass distribution of the BH LMXB population; Özel et al. 2010, where $L_{\rm Edd} = 1.26 \times 10^{38}\,(M_{\rm BH}/{\rm M}_{\odot})$ erg s^{-1}), and our first radio detection occurred at $L_{\rm r} \approx 4.2 \times 10^{29}$ erg s^{-1}. At the X-ray peak of the outburst, GX 339−4 reached an X-ray luminosity of $\sim 4 \times 10^{37}$ erg s^{-1}, corresponding to $L_{\rm Edd} \sim 0.04$. See also Wang et al. (2020) for a discussion on the X-ray luminosity determined with *NICER* (while our results generally agree, their results are taken from observations averaged over multiple days, making a direct comparison difficult). In the radio band, we measured a maximum luminosity of $\sim 2 \times 10^{30}$ erg s^{-1}.

As expected, at its X-ray and radio peak, this outburst was significantly fainter than luminosities reached from successful outbursts of GX 339−4 (Corbel et al. 2013a), as well as those from other systems, where successful outburst luminosities usually exceed 10^{38} erg s^{-1} (Tetarenko et al. 2016). In comparison to other hard-only outbursts from GX 339−4, the 2017–2018 outburst reached similar X-ray luminosities to other hard-only outbursts, within a factor of a few. The observed GX 339−4 luminosities were also in broad agreement with typical peak luminosities from the full sample of hard-only outbursts from other systems ($L_{\rm X} \sim 10^{35}$–10^{37} erg s^{-1}; Tetarenko et al. 2016), albeit on the higher end of that range. Additionally, the

[10]See Russell et al. 2019a for full details on the X-ray Binary New Early Warning System (XB-NEWS).

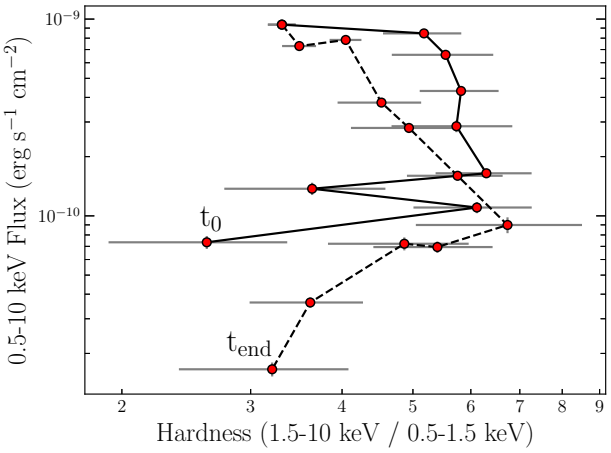

Figure 4. Hardness–intensity diagram of the 2017–2018 outburst, calculated using *Swift*-XRT data. Here, the hardness is defined as the 1.5–10 keV flux over the 0.5–1.5 keV flux. The first *Swift*-XRT observation is marked with t_0 and the last observation with t_{end}. The solid black line represents the rise phase of the outburst, while the dashed black line characterizes the decay. The outburst showed a softer X-ray spectrum at lower X-ray luminosities. Additionally, the source did not evolve to the soft X-ray spectral state in the outburst, but did soften marginally close to the outburst peak.

2017–2018 peak X-ray luminosity occurred at a similar luminosity to the expected hard state to HIMS transition luminosity for a large sample of BH LMXBs ($\geq 0.03 L_{\rm Edd}$; Maccarone 2003; Dunn et al. 2010; Kalemci et al. 2013; Vahdat Motlagh, Kalemci & Maccarone 2019), but below the typical transition luminosities observed from GX 339−4 ($\sim$0.04–0.07$L_{\rm Edd}$; Vahdat Motlagh et al. 2019).

4.2 X-ray spectral evolution

During the early stages of our monitoring, at the lowest observed (1–10 keV) X-ray luminosities of the rise phase ($\lesssim 1.3 \times 10^{-3}\ L_{\rm Edd}$), GX 339−4 exhibited a relatively soft X-ray spectrum. As the source brightened, the X-ray spectrum hardened (Fig. 2). This evolution was demonstrated by the variable changes in the source hardness (Fig. 4) and the X-ray photon index, where Γ evolved back and forth between $\sim$1.7 and $\sim$1.2 over a few days; see Table 1. Following this erratic evolution, at X-ray luminosities of $\gtrsim 1.3 \times 10^{-3}\ L_{\rm Edd}$, Γ increased progressively to $\approx$1.6 at the peak flux of the outburst. As the outburst faded, Γ hardened. Similar to the early stages of the outburst, at the lowest observed X-ray luminosities at the end of the outburst ($\lesssim 7 \times 10^{-4}\ L_{\rm Edd}$), the X-ray spectrum again softened, although this decay phase evolution was much more gradual than during the rise phase. While the gradual softening and hardening of the X-ray spectrum during the bright phase of an outburst is standard, spectral hardening at low X-ray luminosities in the rise phase is generally not observed, although, as we discuss below, this is likely due to a lack of monitoring at such low X-ray luminosities early in the outburst.

In their quiescent state, BH LMXBs show softer X-ray spectra, such that $\Gamma \approx 2$ (e.g. Plotkin et al. 2013; Reynolds et al. 2014). GX 339−4 was not in quiescence during our monitoring (our observations begin at an X-ray luminosity of $\sim 10^{-3}\ L_{\rm Edd}$, well above the expected quiescence level of $\sim 10^{-5}\ L_{\rm Edd}$ for GX 339−4 (Plotkin et al. 2013). It has been suggested that at low X-ray luminosities, the X-ray spectrum could be dominated by emission from the base of the jet (e.g. Markoff et al. 2005; Maitra et al. 2009; Connors et al. 2019; Lucchini et al. 2019), where changes to the observed spectrum could arise from a change in the location of the synchrotron cooling break, $\nu_{\rm cool}$, which represents the frequency at which the radiation time-scales of the synchrotron emission are shorter than the dynamical time-scales of the emitting electrons.[11] While the shape of the X-ray spectrum alone may suggest that the low-luminosity X-ray emission could have been dominated by the un-cooled optically thin emission from the jet,[12] using broad-band *NuSTAR* X-ray observations, García et al. (2019) detected strong signatures of X-ray reprocessing on 2017-10-02 (see also Wang et al. 2020), which are not expected if the X-ray emission is synchrotron in origin (Markoff & Nowak 2004). Instead, García et al. (2019) proposed that the reprocessing originated in an optically thick medium, presumably the accretion disc. In such a case, changes to the optical depth of the disc would have produced observable changes in the X-ray spectrum (such that an increasing optical depth would enhance the high-energy 'hard' X-ray photons) at luminosities similar to our observations (e.g. Yan, Xie & Zhang 2020). As such, rapid changes to the optical depth and geometry (Wang et al. 2020) of the accretion disc could result in the erratic spectral evolution we observed during the low-luminosity stage of the outburst rise. In addition, a further argument against synchrotron cooled X-rays is that they are expected to yield a steeper correlation between the radio and X-ray luminosities (Yuan & Cui 2005), which we did not observe, instead detecting a shallower correlation (see Section 4.3 for results and further discussion).

Alternatively, similar changes to the X-ray spectral shape could also be observed from an optically thin flow in an RIAF (e.g. Narayan & Yi 1995; Esin et al. 1997; Yuan & Narayan 2014). In such a case, if the X-ray emission arises via inverse Compton in the outer disc or synchrotron self-Compton in the inner flow, then both gradual and erratic changes in the X-ray spectrum can be produced simply by changes to the optical depth of the inverse Compton scatterings (e.g. Esin et al. 1997). As such, the X-ray observations imply that the X-ray spectral changes were a result of an evolving optical depth of the accretion flow, whether it is optically thick or thin.

We do note that during the low-luminosity decay phase (from 2018-02-04 and on-wards) our monitoring does not allow us to identify the origin of the hard X-ray emission. García et al. (2019) find signatures of X-ray reprocessing on 2018-01-30, but there were no high spectral resolution X-ray observations after those times. Therefore, it might be possible that the hard X-rays were dominated by emission from the base of the jet at later times.

4.2.1 *Comparison with other outbursts*

A simple comparison of the X-ray spectral evolution against the 2013 hard-only outburst and 2018–2019 hard-only flare from GX 339−4 (Fig. 5) does not show a softer X-ray spectral evolution compared to the 2017–2018 outburst. However, the spectral softening and variability during the earliest stages of our monitoring do not appear to have been observed in these other hard-only outbursts, although, as shown below, this is due to missing data early on in these outbursts.

[11] The position and evolution of the cooling break are very poorly understood; its location has been inferred in the X-ray band at $\sim 10^{-3}\ L_{\rm Edd}$, in the UV-band at $\sim 10^{-5}\ L_{\rm Edd}$ when the source enters quiescence (Pe'er & Markoff 2012; Russell et al. 2013; Shahbaz et al. 2013), and possibly in the optical band at the highest X-ray luminosities (around the transition from the hard state to the soft state; Russell et al. 2014).

[12] Although we would expect Γ to be close to typical optically thin synchrotron spectral indices (such that $\Gamma \sim 1.5$–1.7, where $\alpha_{\rm thin} = 1 - \Gamma$). Then, when $\nu_{\rm cool}$ would be below the X-ray band, the X-ray spectrum should appear even steeper (steepening by a half, such that $\Gamma \sim 2$–2.2), which we did not observe.

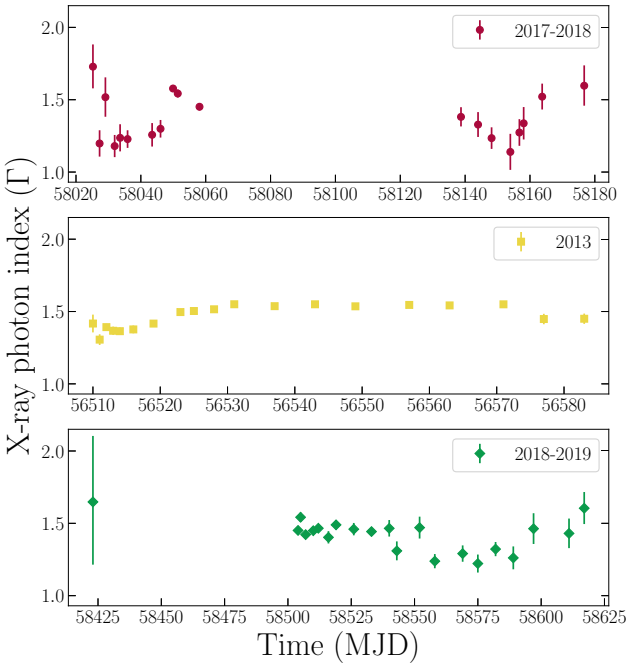

Figure 5. The evolution of the X-ray photon index over time for three different hard-only GX 339−4 outbursts or flaring events. The top panel shows our 2017–2018 outburst. The second and third panels show the 2013 hard-only outburst and 2018–2019 hard-only flare. For all panels the range of photon indices are kept the same for clearer comparison. Note that the early rise part of the 2018–2019 flare was not observed by *Swift*-XRT due to Sun constraints. The X-ray photon index evolution of the 2017–2018 outburst appears somewhat different to the other two failed outbursts shown here, where Γ was initially steep, before flattening as the outburst progressed. Additionally, at the end of the outburst, Γ increased.

To best compare the evolution of the X-ray photon index between outbursts (both hard-only and successful), we explored how Γ evolved with X-ray flux for the 2013 and 2017–2018 hard-only outbursts and 2018–2019 hard-only flare, and a sample of two successful outbursts (Fig. 6). Such a comparison shows clear similarities despite the differences in cadence and luminosity of the observations. At lower X-ray luminosities as the flux increases, Γ first decreases before increasing at higher X-ray fluxes, displaying a regular 'V'-shaped pattern. The only clear difference between the two outburst types is the hysteresis of Γ with X-ray flux: hard-only outbursts appear to traverse the same path during both the rise and decay phases of the outburst, showing little to no hysteresis in Γ (Fig. 6), while successful outbursts appear to follow two different tracks - a harder (lower) track during the rise, and a softer (higher) track during the decay, before re-joining as the source moves to X-ray fluxes $\lesssim 10^{-10}$ erg s^{-1} cm^{-2}. The V-shaped pattern between the X-ray flux and Γ (Fig. 6) at similar luminosities is commonly observed in BH LMXBs (see, e.g. Wu & Gu 2008, Fig. 1). The inflection point, where the source switches from X-ray spectral hardening to softening with increased X-ray luminosity, has been attributed to a transition from an RIAF (at bolometric luminosities of $< 0.01\,L_{\rm Edd}$) to a standard accretion disc ($L_{\rm Bol} > 0.01\,L_{\rm Edd}$; Wu & Gu 2008).

However, other possibilities for the inflection point have also been suggested, such as the point where emission becomes dominated by the jet, or where reprocessed photons begin to dominate in an out-flowing coronal model (e.g. Sobolewska et al. 2011).

To identify any deviation in source behaviour during the Sun constraint, we also compared the X-ray hardness evolution with

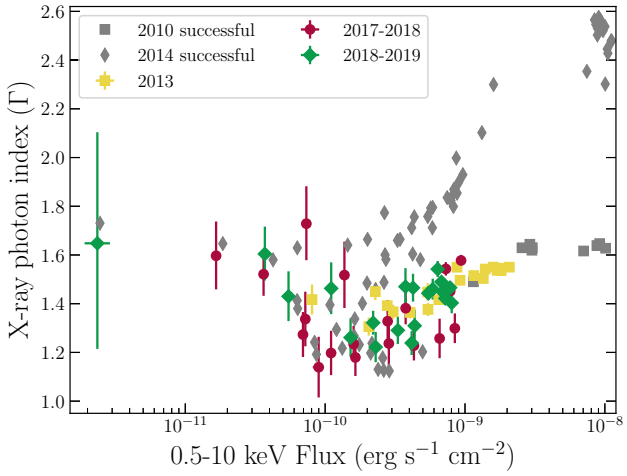

Figure 6. The X-ray photon index versus flux for the 2013 (yellow) and 2017–2018 (red) hard-only outbursts, and the 2018–2019 hard-only flare (green) of GX 339−4, compared to *Swift*-XRT data from the 2010–2011 and 2014–2015 successful outbursts (grey). The evolution during the rise (lower path) and the decay (upper path) appear as two different tracks. This highlights the similarity (during the rise phase) and difference (during the decay phase) in evolution of the X-ray photon index during hard-only and successful outbursts.

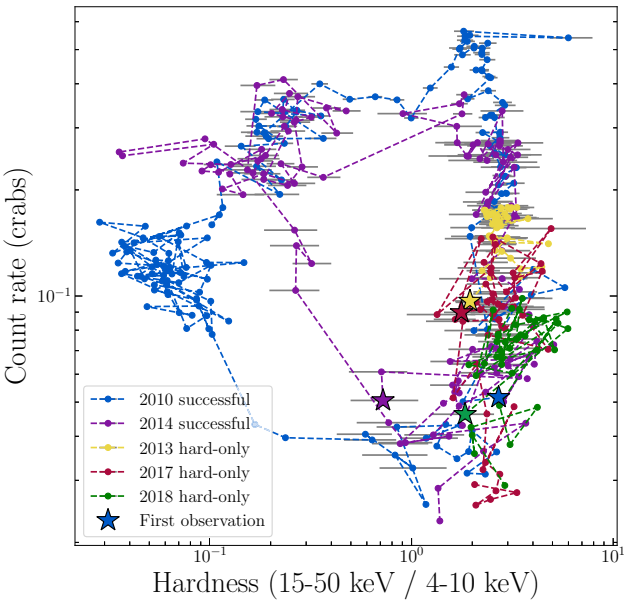

Figure 7. Hardness–intensity diagram for three hard-only events and two successful outbursts from GX 339−4, using data from the *MAXI* X-ray telescope and *Swift*-BAT. Here, we define hardness as the 15–50 keV flux (from *Swift*-BAT) over the 4–10 keV flux (from *MAXI*). The larger stars correspond to the first observations of each outburst. For clarity, we show error bars in grey. This figure indicates that there does not appear to be any significant differences in the *MAXI* and *Swift*-BAT data between hard-only and successful outbursts from GX 339−4 during their rise phases.

X-ray intensity for both hard-only and successful outbursts of this source using *MAXI* and *Swift*-BAT observations (Fig. 7). Our results show that despite showing some minor hysteresis in the *Swift*-XRT data, the 2017–2018 outburst hardness evolution did not appear to significantly deviate from other outbursts of this source. This applies

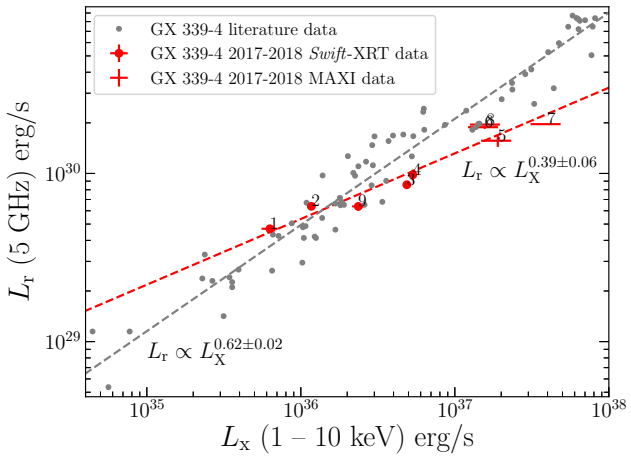

Figure 8. The radio luminosity (L_r) versus X-ray luminosity (L_X) plot of GX 339−4, where the 5 GHz radio luminosity was inferred from the 5.5 GHz radio flux density and the corresponding radio spectral index. The grey points consist of literature outburst data from GX 339−4 (Corbel et al. 2013a), while the red points correspond to data from the 2017–2018 hard-only outburst. The numbers near the red points indicate the order in which the data were obtained, so number 1 corresponds to the first observation of the outburst and number 9 corresponds to the last. As in shown in the figure, for the 2017–2018 outburst, the best-fitting relation is $L_r \propto L_X^{0.39\pm0.06}$, flatter than successful outbursts combined from GX 339−4 (where $L_r \propto L_X^{0.62\pm0.02}$).

to the rise phase of successful outbursts and complete hard-only outbursts.

Therefore, the 2017–2018 X-ray outburst of GX 339−4 seems to follow a relatively typical evolution when compared to the X-ray behaviour of both hard-only and successful outbursts, with no preliminary indicators that may identify whether an outburst is successful or not. A similar result was also found during detailed near-infrared (NIR) and optical studies of outbursts from BH LMXBs (Kosenkov et al. 2020), where no indicators in the NIR/optical colours or magnitude were identified that might allow for an identification of a hard-only or successful outburst.

4.3 The radio–X-ray correlation

With our quasi-simultaneous radio and X-ray data (taken within 1 d of each other),[13] we explored the correlation between the radio and X-ray emission. We used the PYTHON implementation of the linear regression algorithm LINMIX_ERR[14] (Kelly 2007) to perform a (10,000 iteration) linear fit to the radio and X-ray luminosities in logarithmic space, finding a flatter than usual radio–X-ray coupling for GX 339−4, where $L_r \propto L_X^{0.39\pm0.06}$ for this hard-only outburst (Fig. 8). This result included the *MAXI* data which had an assumed value of Γ (where $\Gamma = 1.5$–2.5). However, we note that due to the close proximity of the Sun, the MAXI images were poor. As such, excluding the *MAXI* points did not change our results, providing a best-fitting relation of $L_r \propto L_X^{0.3\pm0.1}$.

A flatter radio–X-ray correlation may suggest a more inefficient coupling between the two emission mechanisms (where the dominant X-ray emission could now arise from synchrotron self-Compton emission from the base of the jet; e.g. Markoff et al. 2005; Corbel, Koerding & Kaaret 2008). An inefficient coupling may arise from a lower mass accretion rate, resulting in a lower magnetic flux and, therefore, possibly weaker jets (e.g. Shibata & Uchida 1987). However, even though the observed relation does deviate significantly from that reported by Corbel et al. (2013a) and Gallo et al. (2012), such a deviation is not necessarily atypical. Corbel et al. (2013a) suggested that over luminosity ranges less than two orders of magnitude, the $L_r - L_X$ correlation index may deviate substantially (where indices of between 0 and 2 have been observed). Here, our radio and X-ray data only span a range of $\lesssim$1 order of magnitude in L_r and $\gtrsim$1.5 orders of magnitude in L_X (Fig. 8).

To extend the X-ray luminosity range, we combined our 2017–2018 $L_r - L_X$ data with radio and X-ray luminosities taken from other hard-only outbursts from GX 339−4 (Fig. 9, left panel), where we include data presented by Corbel et al. 2013a on the 2008, 2009, and 2012 hard-only outbursts. We find a best-fitting relation of $L_r \propto L_X^{0.46\pm0.04}$ ($L_r \propto L_X^{0.44\pm0.07}$ without the *MAXI* data), again much flatter than the $L_r \propto L_X^{0.62\pm0.02}$ relation for the successful outbursts from GX 339−4 (similar to results from Corbel et al. 2013a, who analysed data from five successful and two hard-only outbursts). Performing a Monte Carlo 2-dimensional 2-sample Kolmogorov–Smirnov (K-S) test[15] (Peacock 1983; Fasano & Franceschini 1987) on the successful and hard-only data sets yields a p-value of 0.031, providing statistical evidence that is suggestive that the hard-only and successful radio and X-ray luminosities do not arise from the same parent distribution. Confining the successful outburst data from Corbel et al. (2013a) so that the data are within our observed 2017–2018 radio and X-ray luminosities, we find a best fit of $L_r \propto L_X^{0.61\pm0.04}$ (Fig. 9, right panel), showing that there is not a consistent deviation at these X-ray luminosities.

Our findings indicate that $L_r - L_X$ correlations for hard-only outbursts may be flatter than the correlations exhibited by successful outbursts from GX 339−4, possibly acting as an indicator for outbursts remaining within the hard state. However, our radio and sub-mm monitoring indicate that the compact jet was variable within single observations (Section 3.2.1). Therefore, without strictly simultaneous radio and X-ray observations, such variability may impact our findings. Additionally, Koljonen & Russell (2019) find steeper correlation slopes when the X-ray band is extended from 3–9 to 3–200 keV, but as our comparisons were all made within the same band, our results should not be significantly affected. We note that because the X-ray observations need to span >2 orders of magnitude in luminosity, using this method as a precursor indicator may be impractical (as hard-only outbursts often do not extend to this full range). However, this method may allow some early notification (after ∼1-order of magnitude) that it could be a hard-only outburst, and could also be used to classify unknown historical outbursts, or outbursts with no X-ray spectral or timing observations.

When comparing our result to those from hard-only outbursts of other systems, unfortunately the picture is not very clear. To date, there is a dearth of radio–X-ray monitoring campaigns of both successful and hard-only outbursts from a single source meaning that clear comparisons are difficult to make. One of the only other sources that has been well monitored during both types of outburst is the BH-LMXB H1743−322. However, this system displayed a

[13]The radio/X-ray luminosity data point from MJD 58058 was taken >1 d apart (the mid-point of the X-ray observation was MJD 58058.1, while the ATCA radio observation was MJD 58059.9). Therefore, to best estimate the simultaneous radio luminosity, we fit the radio light curve assuming an exponential rise to estimate the 5.5 GHz flux density at the time of the X-ray observation.

[14]https://github.com/jmeyers314/linmix

[15]https://github.com/syrte/ndtest

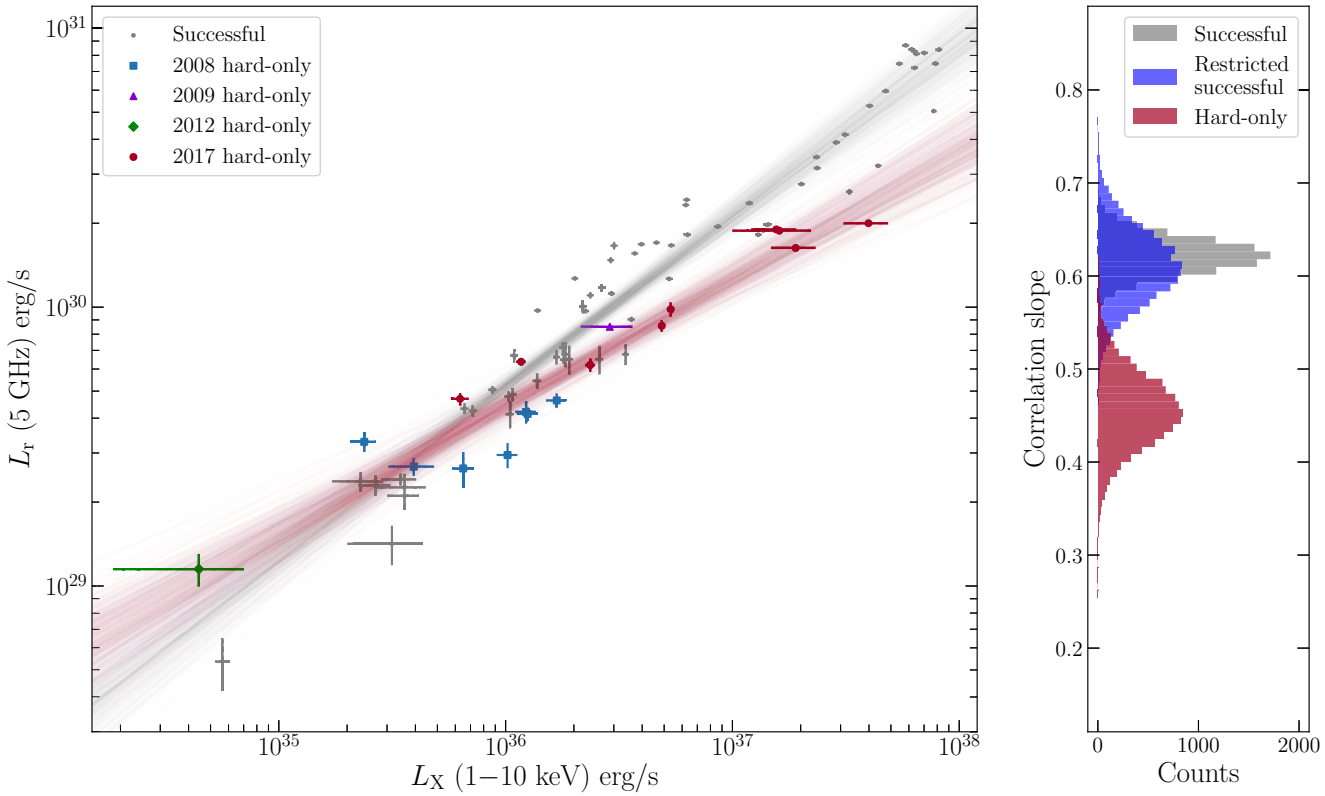

Figure 9. Left-hand panel: The radio and X-ray luminosities of GX 339−4, showing both hard-only outbursts (coloured squares, triangles, diamonds, and circles) and successful outburst data (grey dots). Data from the 2008, 2009, and 2012 hard-only outbursts, as well as the successful outburst luminosities were taken from Corbel et al. (2013a). We determine a best-fitting relation of $L_r \propto L_X^{0.46\pm0.04}$ (red fits), while the successful outburst data have a best fit of $L_r \propto L_X^{0.62\pm0.02}$ (grey fits). Right-hand panel: Histogram showing the fitting results for the successful (grey), restricted successful (blue), and hard-only (red) outburst correlation indexes. These results suggest that hard-only outbursts from GX 339−4 show a flatter radio–X-ray correlation than for successful outbursts.

much more complex radio–X-ray connection, where it lies on the outlier track of the correlation. Sources on the outlier track exhibit a steeper correlation at higher X-ray luminosities, a flatter correlation index at lower X-ray luminosities, and seem to follow the standard correlation track below some critical X-ray luminosity (e.g. Coriat et al. 2011; Koljonen & Russell 2019). As such, for hard-only outbursts (which remain at a relatively low X-ray luminosity) it showed a very shallow correlation (of $L_X^{0.18\pm0.01}$; Jonker et al. 2010), but for successful outbursts, the lower luminosity data follow a similarly shallow path ($L_X^{0.23\pm0.07}$) before transitioning to a much steeper correlation ($L_X^{1.38\pm0.03}$; Coriat et al. 2011). The transition has been attributed to switching between a radiatively efficient and inefficient accretion regime. Williams et al. (2020) presented radio and X-ray observations of H1743−322 during its 2018 hard-only outburst. These observations show that hard-only outbursts can transition between the two paths, following a very similar behaviour. These studies highlight that H1743−322 has appeared to follow the same radio–X-ray correlation path regardless of the outburst being successful or not. Therefore, while GX 339−4 may exhibit a deviance from its standard correlation during hard-only outbursts, such behaviour may not be as clear for the population of BH-LMXB systems, or even for GX 339−4 at higher hard state X-ray luminosities. Therefore, additional monitoring of both types of outburst from the same source with strictly simultaneous radio and X-ray observations is required to identify if a flatter correlation index is indeed a feature of hard-only outbursts from all sources, or if it is something related only to GX 339−4 (or only a subset of BH-LMXBs). In particular, dedicated and more complete monitoring during both the rise and decay are needed, and are now more achievable due to regular optical monitoring (XB-NEWS; Russell et al. 2019a) providing an early trigger for radio and X-ray monitoring.

5 CONCLUSION

Our detailed analysis of X-ray and radio observations taken during the 2017–2018 hard-only outburst of GX 339−4, implied that despite the outburst not entering a soft state, GX 339−4 appeared to show a relatively standard X-ray spectral evolution. While we detected a softer X-ray spectrum at low X-ray luminosities early on in the outburst, using comparisons between both successful and hard-only outbursts from this source we find that this behaviour is normal for both types of outburst (successful and hard-only). We suggest that the changes to the X-ray spectrum during that time were possibly caused by X-ray reprocessing in an optically thick medium, likely the accretion flow, or were due to optical depth changes in an optically thin accretion flow.

Our radio and X-ray monitoring showed a flatter than typical radio–X-ray correlation for this outburst, where $L_r \propto L_X^{0.39\pm0.06}$. Combining our 2017–2018 outburst data with those from other hard-only outbursts from this system also yielded a flatter than typical correlation, where $L_r \propto L_X^{0.46\pm0.04}$, which may arise from a more inefficient coupling between the accretion flow and the jets, possibly due to a lower mass accretion rate. A flatter radio–X-ray

correlation at these lower X-ray luminosities may indicate whether a source completes a full outburst cycle or remains only in the hard state, although extending the luminosity range beyond two orders of magnitude in the X-rays to ensure reliability means that this method may not be a useful precursor indicator, but it could be used to suggest a hard-only outburst as a high possibility early in the outburst (after ∼1 order of magnitude in X-ray luminosity), or for historical and new outbursts with limited X-ray monitoring such that the spectral state changes are not known. However, our radio and X-ray observations were not strictly simultaneous and we detected considerable intra-observational compact jet variability in the sub-mm band (and possibly some in the radio band). Additionally, our results explore a limited luminosity range, focusing on the low-luminosity hard state, which must be extended through better sampling. Also, this behaviour does not necessarily appear to be universal among other systems. Therefore, while a flatter correlation index may act as an indicator for a hard-only outburst from GX 339−4, this may not be the case for other systems. Hence, further monitoring is required to test its universality.

ACKNOWLEDGEMENTS

We thank the anonymous referee for their helpful comments that improved this manuscript. We also thank the UvA Jetset group for useful discussions. TDR acknowledges support from the Netherlands Organisation for Scientific Research (NWO) Veni Fellowship, grant number 639.041.646 and financial contribution from the agreement ASI-INAF n.2017-14-H.0. SM is supported by an NWO Vici grant, grant number 639.043.513. ND, JvdE, and ASP are supported by a Vidi grant from NWO, awarded to ND. JvdE is supported by a Lee Hysan Junior Research Fellowship from St Hilda's College, University of Oxford. GRS acknowledges support from Natural Sciences and Engineering Research Council of Canada (NSERC) Discovery Grants (RGPIN-06569-2016). The Australia Telescope Compact Array (ATCA) is part of the Australia Telescope National Facility which is funded by the Australian Government for operation as a National Facility managed by CSIRO. We acknowledge the Gomeroi people as the traditional owners of the ATCA Observatory site. This paper makes use of the following ALMA data: ADS/JAO.ALMA#2017.1.00864.T. ALMA is a partnership of ESO (representing its member states), NSF (USA), and NINS (Japan), together with NRC (Canada), MOST and ASIAA (Taiwan), and KASI (Republic of Korea), in cooperation with the Republic of Chile. The Joint ALMA Observatory is operated by ESO, AUI/NRAO, and NAOJ. The National Radio Astronomy Observatory is a facility of the National Science Foundation operated under cooperative agreement by Associated Universities, Inc. This research has made use of (i) NASA's Astrophysics Data System, (ii) data, software, and/or web tools obtained from the High Energy Astrophysics Science Archive Research Center (HEASARC), a service of the Astrophysics Science Division at NASA Goddard Space Flight Center (GSFC) and of the Smithsonian Astrophysical Observatory's High Energy Astrophysics Division, (iii) data supplied by the UK *Swift* Science Data Centre at the University of Leicester, and (iiii) *MAXI* data provided by RIKEN, JAXA, and the MAXI team.

DATA AVAILABILITY

Data from *Swift* and *MAXI* are publicly available from HEASARC (https://heasarc.gsfc.nasa.gov/), obsIDs are provided in the data tables. Results and best-fitting parameters are all provided in this paper. Raw radio data can be accessed online (https://atoa.atnf.csiro.au/query.jsp), under project code C3057. Raw ALMA data are available online (https://almascience.eso.org/asax/) under project code 2017.1.00864.T. All radio and sub-mm results are provided in this paper..

REFERENCES

Akritas M. G., Bershady M. A., 1996, ApJ, 470, 706
Aref'ev V. A., Revnivtsev M. G., Lutovinov A. A., Sunyaev R. A., 2004, Astron. Lett., 30, 669
Arnaud K. A., 1996, XSPEC: The First Ten Years. Astronomical Society of the Pacific Conference Series. p. 17
Belloni T., Colombo A. P., Homan J., Campana S., van der Klis M., 2002, A&A, 390, 199
Belloni T. M., 2010, States and Transitions in Black Hole Binaries. Springer, Berlin, p. 53
Bright J. S. et al., 2020, Nat. Astron., 4, 697
Brocksopp C., Bandyopadhyay R. M., Fender R. P., 2004, New Astron., 9, 249
Brocksopp C., Jonker P. G., Fender R. P., Groot P. J., van der Klis M., Tingay S. J., 2001, MNRAS, 323, 517
Brocksopp C., Jonker P. G., Maitra D., Krimm H. A., Pooley G. G., Ramsay G., Zurita C., 2010, MNRAS, 404, 908
Buxton M. M., Bailyn C. D., Capelo H. L., Chatterjee R., Dinçer T., Kalemci E., Tomsick J. A., 2012, AJ, 143, 130
Capitanio F., Belloni T., Del Santo M., Ubertini P., 2009, MNRAS, 398, 1194
Casella P., Pe'er A., 2009, ApJ, 703, L63
Chen W., Shrader C. R., Livio M., 1997, ApJ, 491, 312
Connors R. M. T. et al., 2019, MNRAS, 485, 3696
Corbel S., Coriat M., Brocksopp C., Tzioumis A. K., Fender R. P., Tomsick J. A., Buxton M. M., Bailyn C. D., 2013a, MNRAS, 428, 2500
Corbel S., Fender R. P., 2002, ApJ, 573, L35
Corbel S., Fender R. P., Tomsick J. A., Tzioumis A. K., Tingay S., 2004, ApJ, 617, 1272
Corbel S., Fender R. P., Tzioumis A. K., Nowak M., McIntyre V., Durouchoux P., Sood R., 2000, A&A, 359, 251
Corbel S., Koerding E., Kaaret P., 2008, MNRAS, 389, 1697
Corbel S., Nowak M. A., Fender R. P., Tzioumis A. K., Markoff S., 2003, A&A, 400, 1007
Corbel S. et al., 2013b, MNRAS, 431, L107
Coriat M. et al., 2011, MNRAS, 414, 677
Corral-Santana J. M., Casares J., Muñoz-Darias T., Bauer F. E., Martínez-Pais I. G., Russell D. M., 2016, A&A, 587, A61
Curran P. A., Chaty S., 2013, A&A, 557, A45
Curran P. A. et al., 2014, MNRAS, 437, 3265
Dhawan V., Mirabel I. F., Rodríguez L. F., 2000, ApJ, 543, 373
Dinçer T., Bailyn C. D., Miller-Jones J. C. A., Buxton M., MacDonald R. K. D., 2018, ApJ, 852, 4
Dunn R. J. H., Fender R. P., Körding E. G., Belloni T., Cabanac C., 2010, MNRAS, 403, 61
Díaz Trigo M., Boirin L., 2016, Astron. Nachr., 337, 368
Esin A. A., McClintock J. E., Narayan R., 1997, ApJ, 489, 865
Espinasse M., Fender R., 2018, MNRAS, 473, 4122
Evans P. A. et al., 2009, MNRAS, 397, 1177
Fasano G., Franceschini A., 1987, MNRAS, 225, 155
Fender R., 2006, Jets from X-Ray Binaries. Cambridge Univ. Press, Cambridge, UK, p. 381
Fender R., 2010, 'Disc-Jet' Coupling in Black Hole X-Ray Binaries and Active Galactic Nuclei. Springer-Verlag, Berlin, p. 115
Fender R. P., 2001, MNRAS, 322, 31
Fender R. P., Belloni T. M., Gallo E., 2004, MNRAS, 355, 1105
Fender R. P., Homan J., Belloni T. M., 2009, MNRAS, 396, 1370
Ferrigno C., Bozzo E., Del Santo M., Capitanio F., 2012, A&A, 537, L7
Fürst F. et al., 2015, ApJ, 808, 122
Gallo E., Degenaar N., van den Eijnden J., 2018, MNRAS, 478, L132
Gallo E., Fender R., Kaiser C., Russell D., Morganti R., Oosterloo T., Heinz S., 2005, Nature, 436, 819

Gallo E., Fender R. P., Pooley G. G., 2003, MNRAS, 344, 60
Gallo E., Miller B. P., Fender R., 2012, MNRAS, 423, 590
Gallo E. et al., 2014, MNRAS, 445, 290
García J. A. et al., 2019, ApJ, 885, 48
Hameury J. M., Lasota J. P., McClintock J. E., Narayan R., 1997, ApJ, 489, 234
Hannikainen D., Hunstead R., Campbell-Wilson D., 1998, New Astron. Rev., 42, 601
Harmon B. A. et al., 1994, ApJ, 425, L17
Heida M., Jonker P. G., Torres M. A. P., Chiavassa A., 2017, ApJ, 846, 132
Hjellming R. M., Rupen M. P., 1995, Nature, 375, 464
Hynes R. I., Mauche C. W., Haswell C. A., Shrader C. R., Cui W., Chaty S., 2000, ApJ, 539, L37
Hynes R. I., Steeghs D., Casares J., Charles P. A., O'Brien K., 2003, ApJ, 583, L95
in't Zand J. J. M., Miller J. M., Oosterbroek T., Parmar A. N., 2002, A&A, 394, 553
Jonker P. G. et al., 2010, MNRAS, 401, 1255
Justham S., Schawinski K., 2012, MNRAS, 423, 1641
Kalemci E., Dinçer T., Tomsick J. A., Buxton M. M., Bailyn C. D., Chun Y. Y., 2013, ApJ, 779, 95
Kelly B. C., 2007, ApJ, 665, 1489
Koljonen K. I. I., Russell D. M., 2019, ApJ, 871, 26
Kosenkov I. A., Veledina A., Suleimanov V. F., Poutanen J., 2020, A&A, 638, A127
Lasota J.-P., 2001, New Astron. Rev., 45, 449
Lucchini M., Markoff S., Crumley P., Krauß F., Connors R. M. T., 2019, MNRAS, 482, 4798
Maccarone T. J., 2003, A&A, 409, 697
Maitra D., Markoff S., Brocksopp C., Noble M., Nowak M., Wilms J., 2009, MNRAS, 398, 1638
Markoff S., Nowak M. A., 2004, ApJ, 609, 972
Markoff S., Nowak M. A., Wilms J., 2005, ApJ, 635, 1203
Martí-Vidal I., Vlemmings W. H. T., Muller S., Casey S., 2014, A&A, 563, A136
Massardi M., Bonaldi A., Bonavera L., López-Caniego M., de Zotti G., Ekers R. D., 2011, MNRAS, 415, 1597
Matsuoka M. et al., 2009, PASJ, 61, 999
McClintock J. E., Remillard R. A., 2006, Black Hole Binaries. Cambridge Univ. Press, Cambridge, UK, p. 157
McConnell D., Sadler E. M., Murphy T., Ekers R. D., 2012, MNRAS, 422, 1527
McMullin J. P., Waters B., Schiebel D., Young W., Golap K., 2007, CASA Architecture and Applications. p. 127
Meyer-Hofmeister E., Meyer F., 2014, A&A, 562, A142
Miller-Jones J. C. A. et al., 2012, MNRAS, 421, 468
Mirabel I. F., Dijkstra M., Laurent P., Loeb A., Pritchard J. R., 2011, A&A, 528, A149
Mirabel I. F., Rodriguez L. F., Cordier B., Paul J., Lebrun F., 1992, Nature, 358, 215
Mirabel I. F., Rodríguez L. F., 1994, Nature, 371, 46
Murphy T. et al., 2010, MNRAS, 402, 2403
Narayan R., McClintock J. E., Yi I., 1996, ApJ, 457, 821
Narayan R., Yi I., 1995, ApJ, 452, 710
Özel F., Psaltis D., Narayan R., McClintock J. E., 2010, ApJ, 725, 1918
Paice J. A., Belloni T., Motta S., Gandhi P., Rao A., Misra R., Russell D. M., Charles P., 2020, Astron. Telegram, 13447, 1
Parikh A. S., Russell T. D., Wijnands R., Miller-Jones J. C. A., Sivakoff G. R., Tetarenko A. J., 2019, ApJ, 878, L28
Partridge B., López-Caniego M., Perley R. A., Stevens J., Butler B. J., Rocha G., Walter B., Zacchei A., 2016, ApJ, 821, 61
Peacock J. A., 1983, MNRAS, 202, 615
Pe'er A., Markoff S., 2012, ApJ, 753, 177
Pietka M., Fender R. P., Keane E. F., 2015, MNRAS, 446, 3687
Plotkin R. M., Gallo E., Jonker P. G., 2013, ApJ, 773, 59
Plotkin R. M. et al., 2017, ApJ, 848, 92
Ponti G., Fender R. P., Begelman M. C., Dunn R. J. H., Neilsen J., Coriat M., 2012, MNRAS, 422, L11
Pringle J. E., Rees M. J., Pacholczyk A. G., 1973, A&A, 29, 179
Rao A., Paice J. A., Russell D. M., Gand hi P., Motta S., Lewis F., Misra R., Buckley D. A., 2019, Astron. Telegram, 13113, 1
Reis R. C., Miller J. M., Reynolds M. T., Fabian A. C., Walton D. J., 2012, ApJ, 751, 34
Remillard R. A., McClintock J. E., 2006, ARA&A, 44, 49
Reynolds M. T., Reis R. C., Miller J. M., Cackett E. M., Degenaar N., 2014, MNRAS, 441, 3656
Rushton A. P. et al., 2017, MNRAS, 468, 2788
Russell D. M., Lewis F., Gandhi P., 2017, Astron. Telegram, 10797, 1
Russell D. M. et al., 2013, MNRAS, 429, 815
Russell D. M. et al., 2019a, Astron. Nachr., 340, 278
Russell T. D., Soria R., Miller-Jones J. C. A., Curran P. A., Markoff S., Russell D. M., Sivakoff G. R., 2014, MNRAS, 439, 1390
Russell T. D. et al., 2015, MNRAS, 450, 1745
Russell T. D. et al., 2019b, ApJ, 883, 198
Sadler E. M. et al., 2006, MNRAS, 371, 898
Shahbaz T., Russell D. M., Zurita C., Casares J., Corral-Santana J. M., Dhillon V. S., Marsh T. R., 2013, MNRAS, 434, 2696
Shibata K., Uchida Y., 1987, PASJ, 39, 559
Sidoli L., Paizis A., Mereghetti S., Götz D., Del Santo M., 2011, MNRAS, 415, 2373
Sobolewska M. A., Papadakis I. E., Done C., Malzac J., 2011, MNRAS, 417, 280
Soleri P. et al., 2013, MNRAS, 429, 1244
Sood R., Campbell-Wilson D., 1994, IAU Circ., 6006, 1
Sturner S. J., Shrader C. R., 2005, ApJ, 625, 923
Tetarenko A. J., Casella P., Miller-Jones J. C. A., Sivakoff G. R., Tetarenko B. E., Maccarone T. J., Gand hi P., Eikenberry S., 2019b, MNRAS, 484, 2987
Tetarenko A. J., Freeman P., Rosolowsky E. W., Miller-Jones J. C. A., Sivakoff G. R., 2018, MNRAS, 475, 448
Tetarenko A. J., Rosolowsky E. W., Miller-Jones J. C. A., Sivakoff G. R., 2020, MNRAS, 497, 3504
Tetarenko A. J. et al., 2015, ApJ, 805, 30
Tetarenko A. J. et al., 2017, MNRAS, 469, 3141
Tetarenko A. J. et al., 2019a, MNRAS, 482, 2950
Tetarenko B. E., Sivakoff G. R., Heinke C. O., Gladstone J. C., 2016, ApJS, 222. p. 15
Tingay S. J. et al., 1995, Nature, 374, 141
Vahdat Motlagh A., Kalemci E., Maccarone T. J., 2019, MNRAS, 485, 2744
Vaughan S., Edelson R., Warwick R. S., Uttley P., 2003, MNRAS, 345, 1271
Verner D. A., Ferland G. J., Korista K. T., Yakovlev D. G., 1996, ApJ, 465, 487
Wang J. et al., 2020, ApJ, 899, 44
Wijnands R., Miller J. M., 2002, ApJ, 564, 974
Williams D. R. A. et al., 2020, MNRAS, 491, L29
Wilms J., Allen A., McCray R., 2000, ApJ, 542, 914
Wu Q., Gu M., 2008, ApJ, 682, 212
Yan Z., Xie F.-G., Zhang W., 2020, ApJ, 889, L18
Yuan F., Cui W., 2005, ApJ, 629, 408
Yuan F., Narayan R., 2014, ARA&A, 52, 529
Zdziarski A. A., Gierliński M., Mikołajewska J., Wardziński G., Smith D. M., Harmon B. A., Kitamoto S., 2004, MNRAS, 351, 791
Zdziarski A. A., Ziółkowski J., Mikołajewska J., 2019, MNRAS, 488, 1026
Zhou J. N., Liu Q. Z., Chen Y. P., Li J., Qu J. L., Zhang S., Gao H. Q., Zhang Z., 2013, MNRAS, 431, 2285

APPENDIX A: X-RAY OBSERVATION IDS AND FITTED PARAMETERS

Fitted X-ray parameters and observation identification numbers (obsID) for all *Swift*-XRT data from the 2013 hard-only outburst (Table A1) and 2018–2019 hard-only flare (Table A2).

Table A1. X-ray evolution of GX 339−4 during its 2013 hard-only outburst. These parameters were determined from *Swift*-XRT monitoring, where $N_{\rm H} = (0.56 \pm 0.01) \times 10^{22}$ cm^{-2}. The total χ^2 for the joint fit is 8602.36 with 8619 degrees of freedom. Errors are 1σ.

Date	MJD	ObsID	Count rate (0.5–10 keV)	Γ	Normalization	Unabsorbed flux (0.5–10 keV) $\times 10^{-10}$ erg s^{-1} cm^{-2}
2013–08–06	56510	00032490012	1.21 ± 0.04	1.42 ± 0.06	0.009 ± 0.001	0.81 ± 0.03
2013–08–07	56511	00032898001	2.84 ± 0.06	1.31 ± 0.03	0.021 ± 0.001	2.05 ± 0.05
2013–08–08	56512	00032490013	4.07 ± 0.05	1.39 ± 0.02	0.031 ± 0.001	2.78 ± 0.04
2013–08–09	56513	00032898002	4.53 ± 0.07	1.37 ± 0.03	0.033 ± 0.001	3.06 ± 0.06
2013–08–10	56514	00032490014	5.77 ± 0.08	1.36 ± 0.03	0.044 ± 0.001	4.05 ± 0.07
2013–08–12	56516	00032490015	4.63 ± 0.07	1.38 ± 0.03	0.060 ± 0.002	5.44 ± 0.10
2013–08–15	56519	00032898005	9.60 ± 0.09	1.42 ± 0.02	0.075 ± 0.001	6.49 ± 0.08
2013–08–19	56523	00032898006	13.90 ± 0.12	1.50 ± 0.02	0.117 ± 0.002	9.22 ± 0.10
2013–08–21	56525	00032898007	10.54 ± 0.11	1.50 ± 0.02	0.172 ± 0.003	13.51 ± 0.17
2013–08–24	56528	00080180002	17.39 ± 0.16	1.52 ± 0.02	0.149 ± 0.003	11.55 ± 0.13
2013–08–27	56531	00032898010	23.55 ± 0.15	1.55 ± 0.01	0.215 ± 0.003	15.95 ± 0.12
2013–09–02	56537	00032898013	24.49 ± 0.15	1.54 ± 0.01	0.226 ± 0.003	17.00 ± 0.12
2013–09–08	56543	00032898016	31.42 ± 0.20	1.55 ± 0.01	0.279 ± 0.004	20.75 ± 0.15
2013–09–14	56549	00032898019	27.09 ± 0.18	1.54 ± 0.01	0.240 ± 0.003	18.12 ± 0.14
2013–09–22	56557	00032898023	26.27 ± 0.15	1.55 ± 0.01	0.238 ± 0.003	17.75 ± 0.12
2013–09–28	56563	00032898026	20.61 ± 0.14	1.54 ± 0.01	0.186 ± 0.003	13.95 ± 0.12
2013–10–06	56571	00032898030	12.74 ± 0.11	1.55 ± 0.02	0.118 ± 0.002	8.77 ± 0.09
2013–10–12	56577	00032898033	7.56 ± 0.15	1.45 ± 0.04	0.065 ± 0.002	5.41 ± 0.13
2013–10–18	56583	00032898036	3.34 ± 0.06	1.45 ± 0.04	0.027 ± 0.001	2.29 ± 0.05

Table A2. X-ray evolution of GX 339−4 during its 2018–2019 hard-only flare. These parameters were determined from *Swift*-XRT monitoring, where $N_{\rm H} = (0.56 \pm 0.01) \times 10^{22}$ cm^{-2}. The total χ^2 for the joint fit is 3952.25 with 4163 degrees of freedom, the reduced χ^2 for the joint fit is then $\simeq 0.95$. Errors are 1σ.

Date	MJD	ObsID	Count rate (0.5–10 keV)	Γ	Normalization	Unabsorbed flux (0.5–10 keV) $\times 10^{-10}$ erg s^{-1} cm^{-2}
2018–11–01	58423	00032898181	0.028 ± 0.004	1.65 ± 0.44	0.0004 ± 0.0001	0.024 ± 0.005
2019–01–21	58504	00032898182	11.19 ± 0.11	1.45 ± 0.02	0.089 ± 0.002	7.39 ± 0.09
2019–01–22	58505	00032898183	10.21 ± 0.17	1.54 ± 0.03	0.085 ± 0.003	6.38 ± 0.13
2019–01–24	58507	00032898184	10.88 ± 0.14	1.42 ± 0.02	0.084 ± 0.002	7.23 ± 0.11
2019–01–27	58510	00032898185	10.39 ± 0.11	1.45 ± 0.02	0.083 ± 0.002	6.93 ± 0.09
2019–01–29	58512	00032898186	10.27 ± 0.10	1.47 ± 0.02	0.096 ± 0.002	7.83 ± 0.09
2019–02-02	58516	00032898188	4.67 ± 0.11	1.40 ± 0.04	0.091 ± 0.004	8.03 ± 0.22
2019–02–05	58519	00032898189	10.60 ± 0.10	1.49 ± 0.02	0.085 ± 0.002	6.79 ± 0.08
2019–02–12	58526	00032898190	7.47 ± 0.16	1.46 ± 0.04	0.071 ± 0.003	5.88 ± 0.16
2019–02–19	58533	00032898191	8.37 ± 0.12	1.44 ± 0.03	0.065 ± 0.002	5.47 ± 0.09
2019–02–26	58540	00032898194	6.65 ± 0.20	1.46 ± 0.06	0.052 ± 0.003	4.25 ± 0.15
2019–03–01	58543	00032898195	6.34 ± 0.23	1.31 ± 0.07	0.044 ± 0.003	4.36 ± 0.20
2019–03–10	58552	00032898199	5.98 ± 0.23	1.47 ± 0.08	0.046 ± 0.003	3.75 ± 0.18
2019–03–16	58558	00032898202	0.83 ± 0.02	1.24 ± 0.05	0.038 ± 0.002	4.16 ± 0.15
2019–03–27	58569	00032898205	0.52 ± 0.02	1.29 ± 0.06	0.033 ± 0.002	3.31 ± 0.13
2019–04–02	58575	00032898206	0.61 ± 0.02	1.22 ± 0.06	0.021 ± 0.001	2.30 ± 0.10
2019–04–09	58582	00032898207	0.68 ± 0.02	1.32 ± 0.05	0.023 ± 0.001	2.20 ± 0.08
2019–04–16	58589	00032898208	0.51 ± 0.02	1.26 ± 0.08	0.014 ± 0.001	1.52 ± 0.08
2019–04–24	58597	00032898209	0.39 ± 0.02	1.46 ± 0.11	0.013 ± 0.001	1.10 ± 0.07
2019–05–08	58611	00032898211	0.52 ± 0.03	1.43 ± 0.10	0.006 ± 0.001	0.55 ± 0.04
2019–05–14	58617	00032898212	0.40 ± 0.02	1.60 ± 0.11	0.005 ± 0.001	0.37 ± 0.02

APPENDIX B: RADIO AND SUB-MM VARIABILITY

Intra-observation light curves for the ATCA radio (Table B1 and Fig. B1) and ALMA sub-mm observations (Table B2 and Fig. B2).

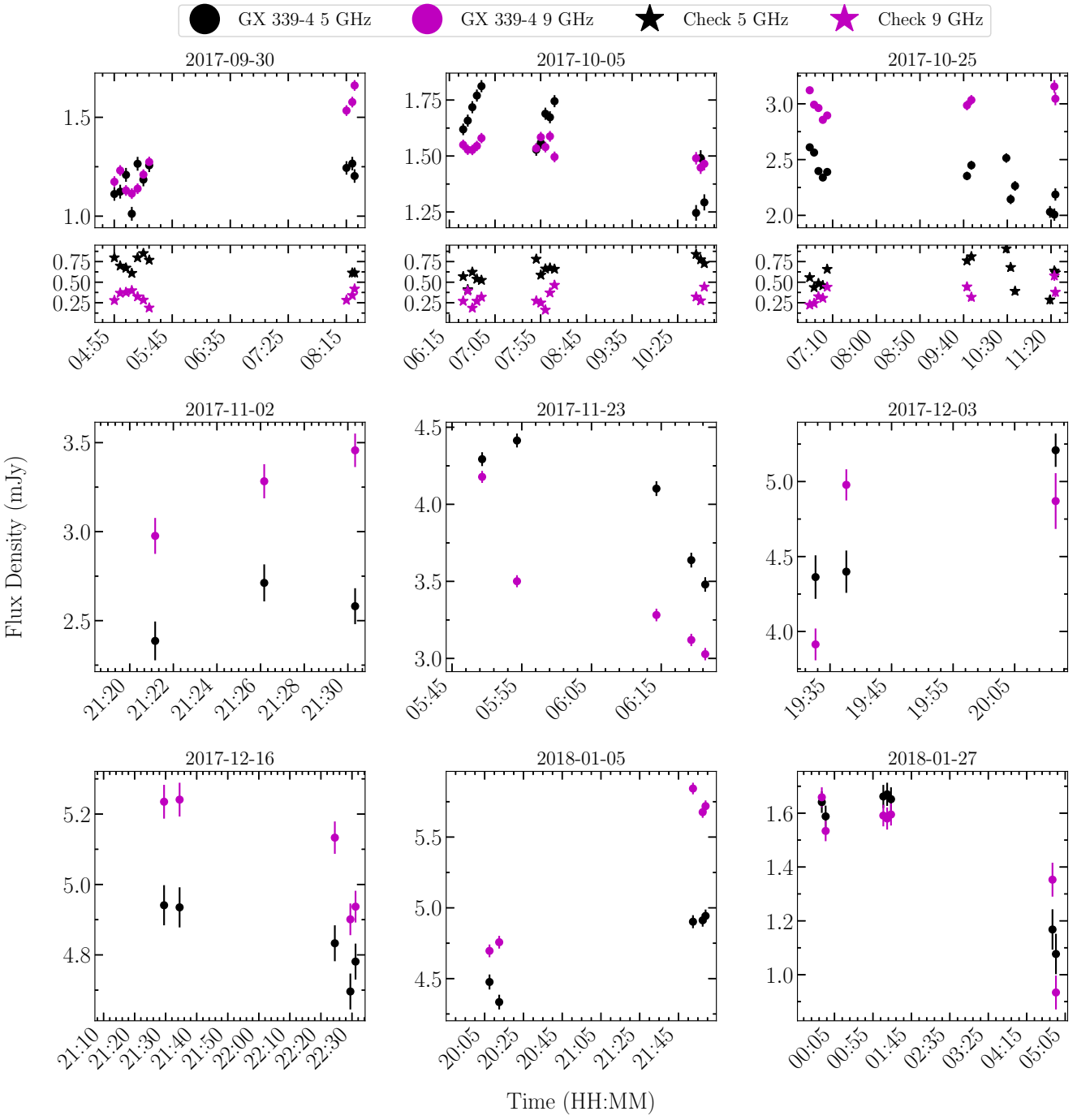

Figure B1. Time-resolved radio light curves of GX 339–4 observed with ATCA at 5 and 9 GHz (black and magenta circles). We also show light curves of a check source in the ATCA field of view for three epochs when this source was detected (black and magenta stars). The radio emission we observe from GX 339–4 shows some short-time-scale variability, in the form of increasing/decreasing trends within (e.g. 2017-10-05) and throughout some observations (e.g. 2017-09-30 and 2017-11-23), but no clear flaring activity. However, we caution that our check source can at times be just as variable as GX 339–4, which suggests that the variations we observe in GX 339-4 may not be completely intrinsic to the source.

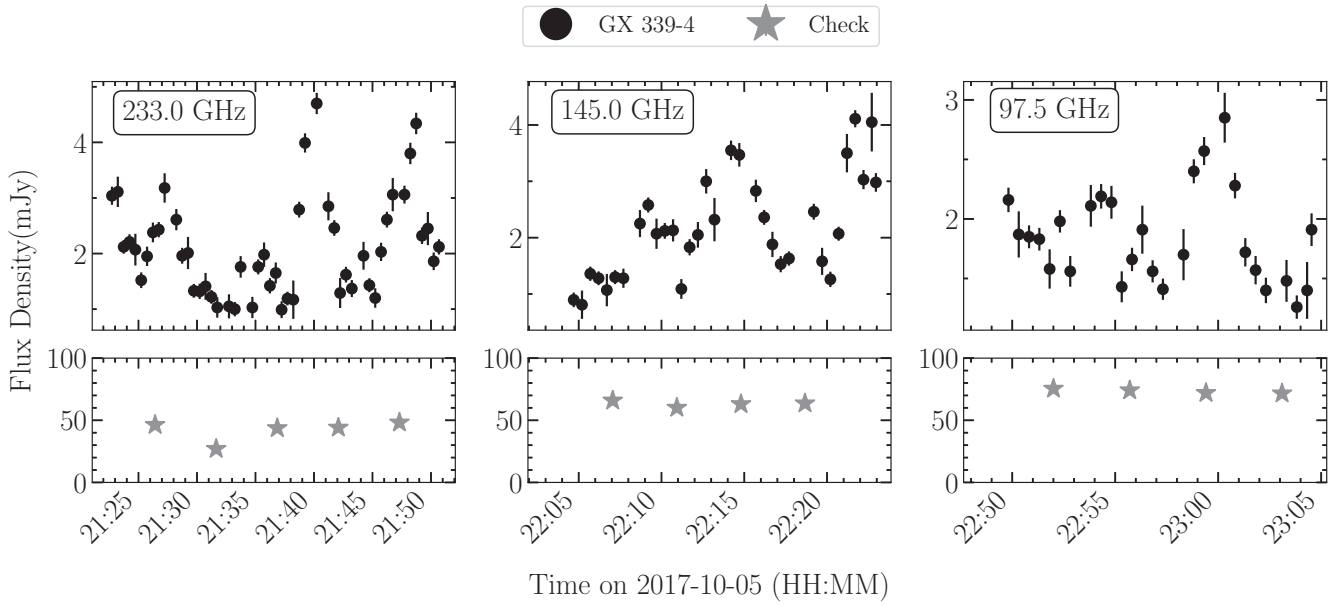

Figure B2. Time-resolved sub-mm light curves of GX 339−4 observed with ALMA at 97.5, 145, and 233 GHz (top panels, black circles). We also show light curves of the check source, J1631–5256 (bottom panels, each grey star is a single ∼20 s scan on the check source). The sub-mm emission we observe from GX 339−4 is clearly variable, where we observe multiple structured flaring events in all the sampled bands. The check source remains relatively constant throughout the observations (any variations are <10 per cent of the average flux density of the check source), indicating that the variability we observe in GX 339−4 is likely intrinsic to the source, and not due to atmospheric or instrumental effects.

Table B1. The time-resolved ATCA radio data of GX 339−4 for each of the observational epochs. The MJD represents the mid-point of the 5-min snapshot.

Epoch	MJD	Central frequency (GHz)	S_ν (mJy)	Error (mJy)
2017-09-30	58026.20496527777	5.5	1.112	0.034
	58026.20843750001	5.5	1.124	0.035
	58026.211909722224	5.5	1.209	0.035
	58026.21538194444	5.5	1.012	0.035
	58026.21885416666	5.5	1.265	0.035
	58026.222326388895	5.5	1.185	0.034
	58026.22579861112	5.5	1.257	0.034
	58026.34385416666	5.5	1.244	0.034
	58026.347326388895	5.5	1.266	0.034
	58026.348715277774	5.5	1.203	0.034
	58026.20496527777	9.0	1.174	0.028
	58026.20843750001	9.0	1.231	0.027
	58026.211909722224	9.0	1.130	0.027
	58026.21538194444	9.0	1.114	0.027
	58026.21885416666	9.0	1.139	0.027
	58026.222326388895	9.0	1.21	0.027
	58026.22579861112	9.0	1.274	0.027
	58026.34385416666	9.0	1.534	0.027
	58026.347326388895	9.0	1.577	0.027
	58026.348715277774	9.0	1.661	0.027
2017-10-05	58031.27093750001	5.5	1.619	0.026
	58031.274409722224	5.5	1.66	0.027
	58031.27788194444	5.5	1.720	0.027
	58031.28135416666	5.5	1.770	0.027
	58031.28482638889	5.5	1.812	0.027
	58031.32649305556	5.5	1.528	0.027
	58031.32996527777	5.5	1.560	0.027
	58031.33343750001	5.5	1.689	0.027
	58031.336909722224	5.5	1.673	0.027
	58031.34038194444	5.5	1.745	0.027
	58031.44802083333	5.5	1.246	0.035

Table B1 *– continued*

Epoch	MJD	Central frequency (GHz)	S_ν (mJy)	Error (mJy)
	58031.45149305556	5.5	1.491	0.035
	58031.45427083333	5.5	1.293	0.036
	58031.27093750001	9.0	1.550	0.023
	58031.274409722224	9.0	1.528	0.023
	58031.27788194444	9.0	1.527	0.023
	58031.28135416666	9.0	1.545	0.023
	58031.28482638889	9.0	1.580	0.023
	58031.32649305556	9.0	1.534	0.024
	58031.32996527777	9.0	1.584	0.024
	58031.33343750001	9.0	1.540	0.024
	58031.336909722224	9.0	1.588	0.024
	58031.34038194444	9.0	1.496	0.024
	58031.44802083333	9.0	1.490	0.028
	58031.45149305556	9.0	1.450	0.028
	58031.45427083333	9.0	1.465	0.029
2017-10-25	58051.280428240745	5.5	2.61	0.028
	58051.28390046296	5.5	2.563	0.028
	58051.2873726852	5.5	2.397	0.028
	58051.29084490741	5.5	2.339	0.028
	58051.29431712962	5.5	2.390	0.028
	58051.405428240745	5.5	2.353	0.038
	58051.40890046296	5.5	2.449	0.039
	58051.43667824073	5.5	2.514	0.042
	58051.44015046296	5.5	2.144	0.043
	58051.44362268518	5.5	2.264	0.043
	58051.47140046296	5.5	2.031	0.053
	58051.4748726852	5.5	2.007	0.055
	58051.47568287038	5.5	2.187	0.055
	58051.280428240745	9.0	3.121	0.032
	58051.28390046296	9.0	2.992	0.032
	58051.2873726852	9.0	2.962	0.031
	58051.29084490741	9.0	2.856	0.032
	58051.29431712962	9.0	2.895	0.031
	58051.405428240745	9.0	2.986	0.044
	58051.40890046296	9.0	3.034	0.044
	58051.4748726852	9.0	3.155	0.057
	58051.47568287038	9.0	3.045	0.058
2017-11-02	58059.889918981484	5.5	2.386	0.109
	58059.89339120369	5.5	2.712	0.104
	58059.89628472223	5.5	2.581	0.101
	58059.889918981484	9.0	2.976	0.101
	58059.89339120369	9.0	3.283	0.096
	58059.89628472223	9.0	3.457	0.094
2017-11-23	58080.242581018516	5.5	4.293	0.045
	58080.246053240735	5.5	4.414	0.045
	58080.259942129625	5.5	4.102	0.048
	58080.263414351844	5.5	3.638	0.048
	58080.26480324073	5.5	3.48	0.047
	58080.242581018516	9.0	4.178	0.039
	58080.246053240735	9.0	3.501	0.039
	58080.259942129625	9.0	3.282	0.041
	58080.263414351844	9.0	3.120	0.040
	58080.26480324073	9.0	3.028	0.040
2017-12-03	58090.814340277764	5.5	4.363	0.145
	58090.81781249999	5.5	4.399	0.141
	58090.84142361111	5.5	5.209	0.111
	58090.814340277764	9.0	3.914	0.106
	58090.81781249999	9.0	4.978	0.104
	58090.84142361111	9.0	4.870	0.186
2017-12-16	58103.89547453704	5.5	4.941	0.057
	58103.898946759255	5.5	4.935	0.057
	58103.93366898148	5.5	4.833	0.051
	58103.93714120369	5.5	4.696	0.051

Table B1 – *continued*

Epoch	MJD	Central frequency (GHz)	S_ν (mJy)	Error (mJy)
	58103.938298611116	5.5	4.781	0.051
	58103.89547453704	9.0	5.235	0.048
	58103.898946759255	9.0	5.241	0.048
	58103.93366898148	9.0	5.133	0.046
	58103.93714120369	9.0	4.901	0.045
	58103.938298611116	9.0	4.937	0.045
2018-01-05	58123.838530092595	5.5	4.476	0.053
	58123.842002314814	5.5	4.334	0.052
	58123.91144675926	5.5	4.902	0.046
	58123.914918981485	5.5	4.912	0.045
	58123.915960648155	5.5	4.943	0.045
	58123.838530092595	9.0	4.696	0.045
	58123.842002314814	9.0	4.757	0.045
	58123.91144675926	9.0	5.843	0.041
	58123.914918981485	9.0	5.676	0.040
	58123.915960648155	9.0	5.719	0.040
2018-01-27	58145.992002314815	5.5	1.641	0.04
	58145.99547453704	5.5	1.588	0.04
	58146.04755787037	5.5	1.662	0.043
	58146.05103009259	5.5	1.670	0.043
	58146.05450231481	5.5	1.652	0.044
	58146.200335648144	5.5	1.168	0.075
	58146.203460648154	5.5	1.077	0.075
	58145.992002314815	9.0	1.659	0.037
	58145.99547453704	9.0	1.534	0.038
	58146.04755787037	9.0	1.591	0.040
	58146.05103009259	9.0	1.580	0.041
	58146.05450231481	9.0	1.595	0.041
	58146.200335648144	9.0	1.353	0.063
	58146.203460648154	9.0	0.934	0.063

Table B2. The time-resolved sub-mm light-curve data of GX 339–4 observed with ALMA at 97.5, 145, and 233 GHz on 2017-10-05. The MJD represents the mid-point of the 30-s snapshot.

MJD	Central frequency (GHz)	S_ν (mJy)	Error (mJy)
58031.891377314816	233.0	3.04	0.16
58031.89172453704	233.0	3.11	0.27
58031.89207175926	233.0	2.12	0.12
58031.89241898148	233.0	2.21	0.14
58031.8927662037	233.0	2.07	0.29
58031.893113425926	233.0	1.52	0.14
58031.89346064815	233.0	1.95	0.17
58031.89380787037	233.0	2.38	0.18
58031.894155092596	233.0	2.43	0.14
58031.89450231481	233.0	3.18	0.26
58031.89519675926	233.0	2.61	0.19
58031.89554398148	233.0	1.96	0.14
58031.895891203705	233.0	2.01	0.29
58031.89623842593	233.0	1.33	0.12
58031.896585648145	233.0	1.32	0.14
58031.89693287037	233.0	1.41	0.24
58031.89728009259	233.0	1.22	0.12
58031.897627314815	233.0	1.03	0.18
58031.89832175926	233.0	1.05	0.22
58031.89866898148	233.0	1.00	0.13
58031.8990162037	233.0	1.76	0.19
58031.89971064815	233.0	1.03	0.19
58031.90005787037	233.0	1.76	0.14
58031.900405092594	233.0	1.98	0.22
58031.90075231481	233.0	1.42	0.14
58031.90109953703	233.0	1.65	0.19
58031.90144675926	233.0	0.99	0.15
58031.90179398148	233.0	1.19	0.12
58031.902141203704	233.0	1.17	0.35
58031.90248842593	233.0	2.79	0.14
58031.90283564815	233.0	3.99	0.17
58031.90353009259	233.0	4.70	0.19
58031.90422453704	233.0	2.85	0.25
58031.90457175926	233.0	2.46	0.14
58031.90491898148	233.0	1.29	0.27
58031.90526620371	233.0	1.62	0.14
58031.90561342592	233.0	1.37	0.15
58031.90630787037	233.0	1.96	0.25
58031.90665509259	233.0	1.43	0.13
58031.907002314816	233.0	1.20	0.18
58031.90734953704	233.0	2.03	0.16
58031.907696759255	233.0	2.61	0.14
58031.90804398148	233.0	3.06	0.30
58031.908738425926	233.0	3.06	0.16
58031.90908564815	233.0	3.80	0.19
58031.90943287037	233.0	4.34	0.19
58031.90978009259	233.0	2.32	0.15
58031.91012731481	233.0	2.45	0.30
58031.910474537035	233.0	1.86	0.16
58031.910787037035	233.0	2.12	0.14
58031.9200462963	145.0	0.90	0.13
58031.920393518514	145.0	0.81	0.25
58031.92074074074	145.0	1.36	0.13
58031.92108796296	145.0	1.28	0.12
58031.921435185184	145.0	1.07	0.29

Table B2 – *continued*

MJD	Central frequency (GHz)	S_ν (mJy)	Error (mJy)
58031.92178240741	145.0	1.30	0.12
58031.92212962963	145.0	1.28	0.17
58031.92282407408	145.0	2.25	0.24
58031.923171296294	145.0	2.58	0.13
58031.92351851852	145.0	2.07	0.27
58031.92386574074	145.0	2.12	0.14
58031.924212962964	145.0	2.13	0.20
58031.92456018519	145.0	1.09	0.18
58031.92490740741	145.0	1.83	0.14
58031.92525462963	145.0	2.05	0.22
58031.92560185185	145.0	3.00	0.22
58031.92594907407	145.0	2.32	0.39
58031.92664351852	145.0	3.55	0.17
58031.92699074074	145.0	3.47	0.21
58031.92768518518	145.0	2.83	0.20
58031.928032407406	145.0	2.36	0.13
58031.92837962963	145.0	1.88	0.22
58031.92872685185	145.0	1.53	0.14
58031.929074074076	145.0	1.63	0.13
58031.93011574074	145.0	2.46	0.14
58031.93046296296	145.0	1.58	0.24
58031.930810185186	145.0	1.26	0.14
58031.93115740741	145.0	2.07	0.12
58031.931504629625	145.0	3.50	0.34
58031.93185185185	145.0	4.11	0.15
58031.93219907407	145.0	3.03	0.17
58031.932546296295	145.0	4.05	0.52
58031.9327199074	145.0	2.98	0.17
58031.95130787037	97.5	2.16	0.10
58031.951655092584	97.5	1.87	0.19
58031.95200231481	97.5	1.85	0.10
58031.95234953703	97.5	1.83	0.10
58031.952696759254	97.5	1.58	0.17
58031.95304398148	97.5	1.98	0.09
58031.9533912037	97.5	1.56	0.13
58031.95408564815	97.5	2.11	0.18
58031.95443287036	97.5	2.19	0.10
58031.95478009259	97.5	2.14	0.14
58031.95512731481	97.5	1.43	0.13
58031.95547453703	97.5	1.66	0.10
58031.95582175926	97.5	1.91	0.20
58031.95616898148	97.5	1.56	0.09
58031.956516203696	97.5	1.41	0.09
58031.95721064814	97.5	1.70	0.22
58031.957557870366	97.5	2.40	0.10
58031.95790509259	97.5	2.57	0.12
58031.958599537036	97.5	2.85	0.21
58031.95894675926	97.5	2.28	0.11
58031.95929398148	97.5	1.72	0.12
58031.959641203706	97.5	1.57	0.12
58031.95998842592	97.5	1.40	0.11
58031.96068287037	97.5	1.48	0.18
58031.96103009259	97.5	1.26	0.10
58031.961377314816	97.5	1.40	0.24
58031.961527777785	97.5	1.91	0.14

This paper has been typeset from a TEX/LATEX file prepared by the author.